Floodwater Impact on Galveston Bay Phytoplankton Taxonomy, Pigment Composition and Photo-Physiological State following Hurricane Harvey from Field and Ocean Color (Sentinel-3A OLCI) Observations

Bingqing Liu[1], Eurico D'Sa[1*] and Ishan Joshi[1]

[1]Department of Oceanography and Coastal Sciences, Louisiana State University, Baton Rouge, LA 70803, USA

* Corresponding author: ejdsa@lsu.edu

Abstract

Phytoplankton taxonomy, pigment composition and photo-physiological state were studied in Galveston Bay (GB), Texas (USA) following the extreme flooding associated with Hurricane Harvey (August 25–29, 2017) using field and satellite ocean color observations. Percentage of chlorophyll a (Chl a) in different phytoplankton groups were determined from a semi-analytical IOP (inherent optical property) inversion algorithm. The IOP inversion algorithm revealed the dominance of freshwater species (diatom, cyanobacteria and green algae) in the bay following the hurricane passage (September 29, 2017) under low salinity conditions associated with the discharge of floodwaters into GB; 2 months after the hurricane (October 29–30, 2017), under more seasonal salinity conditions, the phytoplankton community transitioned to an increase in small sized groups such as haptophyte and prochlorophyte. Sentinel-3A OLCI-derived Chl a obtained using a red/NIR band ratio algorithm for the turbid estuarine waters was highly correlated ($R^2 > 0.90$) to HPLC-derived Chl a concentrations. Long-term observations of OLCI-derived Chl a (August, 2016-December, 2017) in GB revealed that hurricane-induced Chl a declined to background mean state in late October, 2017. A Non-Negative Least Square (NNLS) inversion model was then applied to OLCI-derived Chl a maps of GB to investigate spatiotemporal variations of phytoplankton diagnostic pigments pre- and post-hurricane; results appeared consistent with extracted phytoplankton taxonomic composition derived from the IOP inversion algorithm and microplankton pictures obtained from an Imaging FlowCytobot (IFCB). OLCI-derived diagnostic pigment distributions also exhibited good agreement with HPLC measurements during both surveys, with mean R^2 ranging from 0.40 for diatoxanthin to 0.96 for Chl a. Environmental factors (e.g., floodwaters) combined with phytoplankton taxonomy also strongly modulated phytoplankton physiology in the bay as indicated by measurements of photosynthetic parameters with a Fluorescence Induction and Relaxation (FIRe) system. Phytoplankton in well-mixed waters (mid-bay area) exhibited maximum PSII photochemical efficiency (F_V/F_M) and low effective absorption cross section (σ_{PSII}), while the areas adjacent to the shelf (likely nutrient-limited) showed low F_V/F_M and elevated σ_{PSII} values. Overall, the approach using field and ocean color data combined with inversion models allowed, for the first time, an assessment of phytoplankton response to a large hurricane-related floodwater perturbation in a turbid estuarine environment based on its taxonomy, pigment composition and physiological state.

Key words: Galveston Bay, phytoplankton taxonomy, pigment composition, physiology, ocean color, chlorophyll a, Sentinel-3A OLCI

1. Introduction

Phytoplankton, which form the basis of the aquatic food web, are crucial to marine ecosystems and play a strong role in marine biogeochemical cycling and climate change. Phytoplankton contributes approximately half of the total primary production on Earth, fixing ~50 GT of carbon into organic matter per year through photosynthesis; however, various phytoplankton taxa affect differently the carbon fixation and export (Sathyendranath et al., 2014). Chlorophyll a (Chl a), an essential phytoplankton photosynthetic pigment, has been considered a reliable indicator of phytoplankton biomass and primary productivity in aquatic systems (Bracher et al., 2015). Phytoplankton also contain several accessory pigments such as chlorophyll-b (Chl b), chlorophyll-c (Chl c), photosynthetic carotenoids (PSC) and photo-protective carotenoids (PPC) that are either involved in light harvesting, or in protecting Chl a and other sensitive pigments from photo-damage (Fishwick et al., 2006). Some of PSCs and PPCs are taxa-specific and have been considered as bio-marker pigments: e.g., fucoxanthin (PSC) for diatoms, peridinin (PPC) for certain dinoflagellates, alloxanthin (PPC) for cryptophytes, zeaxanthin (PPC) for prokaryotes (e.g. cyanobacteria), and the degradation products of Chl a, namely, divinyl Chl a and divinyl-Chl b for prochlorophyte (Jeffrey and Vest, 1997). High-Performance Liquid Chromatography (HPLC) which can efficiently detect and quantify several chemo-taxonomically significant chlorophylls and carotenoids, when coupled with these taxa-specific pigment ratios, allow phytoplankton taxonomic composition to be quantified based on a pigment concentration diagnostic procedures such as CHEMTAX (Mackey et al., 1996). Furthermore, phytoplankton pigments with distinct absorption characteristics strongly influence the light absorption by phytoplankton (Bidigare et al., 1990; Ciotti et al., 2002; Bricaud et al., 2004). As such, phytoplankton absorption spectra has been used to infer underlying pigments and also phytoplankton taxonomy by Gaussian-decomposition of (Hoepffner and Sathyendranath, 1991; Lohrenz et al., 2003; Ficek et al., 2004; Chase et al., 2013; Moisan et al., 2013; Wang et al., 2016; Moisan et al., 2017). More importantly, phytoplankton optical properties (absorption and backscattering) bearing the imprints of different pigments and cell-size, are important contributors to reflectance in a waterbody (Gordon et al., 1988). Morel and Prieur, (1977) first reported the feasibility of calculating the phytoplankton absorption coefficients and other inherent optical properties (IOPs) from measured subsurface irradiance reflectance based on the simplified radiative transfer equation. Improvements in semi-analytical inversion algorithms to derive IOPs from in-situ and remotely sensed reflectance spectra have been reported (Roesler and Perry, 1995; Hoge and Lyon, 1996; Lee et al., 1996; Garver and Siegel, 1997; Carder et al., 1999; Maritorena et al., 2002; Roesler and Boss, 2003; Chase et al., 2017). Roesler et al. (2003) further modified an earlier IOP inversion algorithm used in Roesler and Perry, (1995) by adding a set of 5 species-specific phytoplankton absorption spectra, and derived phytoplankton taxonomic composition from the field measured remote sensing reflectance.

Phytoplankton pigment composition varies not only between taxonomic groups but also with photo-physiological state of cells and environmental stress (e.g., light, nutrients, temperature, salinity, turbulence and stratification) (Suggett et al., 2009). The photosynthetic pigment field is an important factor influencing the magnitude of fluorescence emitted by phytoplankton, with active fluorometry commonly used to obtain estimates of phytoplankton biomass (D'Sa et al., 1997). Advanced active fluorometry termed as fast repetition rate (FRR; (Kolber et al., 1998)) and analogous techniques such as the fluorescence induction and relaxation (FIRe; Suggett et al., 2008) allows for the simultaneous measurements of the maximum PSII photochemical efficiency (F_V/F_M; where F_m and F_o is maximum and minimum fluorescence yield and F_v is variable fluorescence obtained by subtracting F_o from F_m) and the effective absorption cross section (σ_{PSII}) of a phytoplankton population; these have been used as diagnostic indicators for the rapid assessment of phytoplankton health and photo-physiological state linked to environmental stressors. Considerable effort has been invested to achieve a deeper understanding of the impacts of environmental factors and phytoplankton taxonomy on photosynthetic performance of natural communities from field and laboratory fluorescence measurements (Kolber et al., 1988; Geider et al., 1993; Schitüter et al., 1997; Behrenfeld and Kolber, 1999; D'Sa and Lohrenz, 1999;

98   Holmboe et al., 1999; Moore et al., 2003). Furthermore, knowledge of photo-physiological responses of
99   phytoplankton in combination with information on phytoplankton taxonomic composition could provide
100 additional insights on regional environmental conditions.

101 Synoptic mapping of aquatic ecosystems using satellite remote sensing has revolutionized our
102 understanding of phytoplankton dynamics at various spatial and temporal scales in response to
103 environmental variabilities and climate change. It has also provided greater understanding of biological
104 response to large events such as hurricanes in oceanic and coastal waters (Babin et al. 2004; Acker et al.
105 2009; D'Sa 2014; Farfan et al. 2014; Hu and Feng, 2016). Although the primary focus of ocean color
106 sensors has been to determine the Chl a concentration and related estimates of phytoplankton primary
107 production (Mitchell, 1994; Behrenfeld and Falkowski, 1997), more recently, several approaches have
108 been developed based on phytoplankton optical signatures to derive spatial distributions of phytoplankton
109 functional types (PFTs) (Alvain et al., 2005; Nair et al., 2008; Hirata et al., 2011), phytoplankton size
110 classification (Ciotti et al., 2002; Hirata et al., 2008; Brewin et al., 2010; Devred et al., 2011), and
111 phytoplankton accessory pigments (Pan et al., 2010; Pan et al., 2011; Moisan et al., 2013; Moisan et al.,
112 2017; Sun et al., 2017). The basis of these satellite-based remote sensing algorithms have relied on
113 distinct spectral contributions from phytoplankton community composition (e.g., taxonomy, size structure)
114 to remote sensing reflectance (R_{rs}, sr^{-1}); however, these studies have all been confined to open ocean and
115 shelf waters. In contrast, satellite studies of phytoplankton pigments have been limited in the optically
116 complex estuarine waters where the influence from wetlands, rivers, and coastal ocean make
117 phytoplankton communities highly variable and complex.

118 In this study, field bio-optical measurements and ocean color remote sensing data (Sentinel-3A OLCI)
119 acquired in Galveston Bay, a shallow estuary along the Gulf coast (Texas, USA; Fig. 1), are used to
120 investigate the spatial distribution of phytoplankton pigments, taxonomic composition, and their photo-
121 physiological state following the extreme flooding of the Houston Metropolitan and surrounding areas
122 due to Hurricane Harvey and the consequent biological impact of the floodwater discharge into the bay.
123 The paper is organized as follows: section 2 describes the field data acquisition and laboratory processing,
124 section 3 presents the algorithms and methods used to distinguish phytoplankton groups, retrieve spatial
125 distribution of pigments, and calibrate phytoplankton physiological parameters. Results and discussions
126 (section 4 and 5), and summary (section 6) addresses the main contributions and findings of this paper.

127
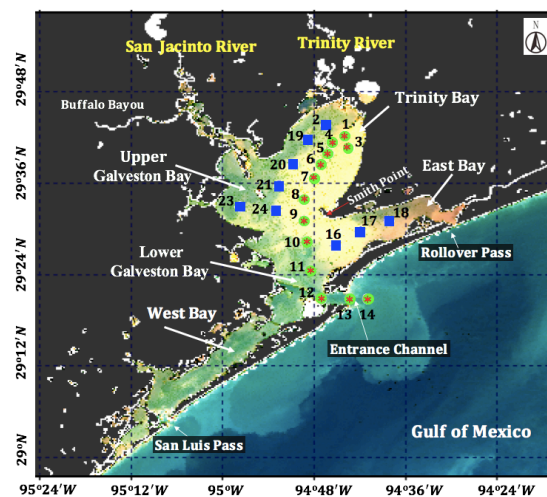
128 **Figure 1**. Sentinel-3A OLCI RGB image (October 29, 2017) with locations of sampling sites in
129 Galveston Bay acquired on September 29 (red asterisk), October 29 (green circles) and October 30 (blue
130 solid squares), 2017, respectively.

2. Data and Methods

2.1 Study area

Galveston Bay (GB), a shallow water estuary (~2.1 m average depth), encompasses two major sub-estuaries: San Jacinto Estuary (also divided as Upper GB and Lower GB), and Trinity Estuary (Trinity Bay) (Fig. 1). It is located adjacent to the heavily urbanized and industrialized metropolitan areas of Houston, Texas (Dorado et al., 2015). A deep (~14 m) narrow Houston Ship Channel connects the bay to the northern Gulf of Mexico (nGoM) through a narrow entrance, the Bolivar Roads Pass. Tidal exchange between GB and the nGoM occurs through the entrance channel with diurnal tides ranging from ~0.15 to ~0.5 m. The major freshwater sources to GB are the Trinity River (55%), the San Jacinto River (16%), and Buffalo Bayou (12%) (Guthrie et al., 2012). The San Jacinto River was frequently observed to transport greater amounts of dissolved nutrients into GB than the Trinity River (Quigg, 2011); however, the negative relationship between nitrate concentrations and salinity observed in the mid-bay area (adjacent to Smith Point) (Santschi, 1995), indicated Trinity River to be a major source of nitrate in GB. The catastrophic flooding of Houston and surrounding areas associated with Hurricane Harvey resulted in strong freshwater inflows into GB from the San Jacinto River (>3300 m^3s^{-1}; USGS 08067650) on August 29, 2017 and the Trinity River (>2500 m^3s^{-1}; USGS 08066500 site at Romayor, Texas) on August 30, 2017, respectively. Although the discharge from the two rivers in the upstream returned to normal conditions (~50–120 m^3s^{-1}) in about 2 weeks after the Hurricane passage, salinity remained low for over a month following the hurricane passage (D'Sa et al., 2018).

2.2 Sampling and Data Collection

Surface water samples were collected at a total of 34 stations during two surveys on September 29 and October 29–30, 2017 (Fig. 1). Samples at stations 1 to 14 (red asterisk on top of green circle; Fig. 1) along the Trinity River transect were collected repeatedly on September 29 and October 29, 2017, respectively. Additional 9 sampling sites (blue squares; Fig. 1) around the upper bay and in the East Bay were sampled on October 30, 2017. The surface water samples were stored in coolers and filtered on the same day. The filter pads were immediately frozen and stored in liquid nitrogen for laboratory absorption spectroscopic and HPLC measurements of the samples. An optical package equipped with a conductivity-temperature-depth recorder (Sea-Bird SBE) and a Fluorescence Induction and Relaxation System (FIRe; Satlantic Inc) was used to obtain profiles of salinity, temperature, pressure, and phytoplankton physiological parameters (F_V/F_M and σ_{PSII}). Measurements of backscattering were also made at each station using the WETLabs VSF-3 (470, 530, 670 nm) backscattering sensor (D'Sa et al. 2006). Included in the optical package was also a hyperspectral downwelling spectral irradiance meter (HyperOCR, Satlantic). The irradiance data from HyperOCR were processed using Prosoft 7.7.14 and the photosynthetically Active Radiation (PAR) were estimated from the irradiance measurements. The above-water reflectance measurements were collected using a GER 1500 512iHR spectroradiometer in the 350-1050 nm spectral range. At each station, sky radiance, plate radiance, and water radiance were recorded (each repeated three times) and processed to obtain above-water remote sensing reflectance (Joshi et al., 2017). A total of 43 Sentinel-3A OLCI full resolution mode, cloud free level-1 images were obtained over GB between August 01, 2016-December 01, 2017 from the European Organization for Meteorological Satellites (EUMESAT) website and pre-processed using Sentinel-3 Toolbox Kit Module (S3TBX) version 5.0.1 in Sentinel Application Platform (SNAP). These Sentinel-3A OLCI data were further atmospherically corrected to obtain remote sensing reflectance ($R_{rs\ OLCI}$, sr^{-1}) using Case-2 Regional Coast Color (C2RCC) module version 0.15 (Doerffer and Schiller, 2007). River discharge information during August, 2016-December, 2017 was downloaded from the USGS Water Data (USGS) for Trinity River at Romayor, Texas (USGS 08066500) and the west flank of the San Jacinto River (USGS 08067650). Individual pictures of microplankton (10 to 150 µm) recorded by an Imaging

177 FlowCytobot (IFCB) located at the entrance to Galveston Bay were downloaded (http://dq-cytobot-
178 pc.tamug.edu/tamugifcb) for pigment validation.

2.3 Absorption Spectroscopy

180 Surface water samples were filtered through 0.2-µm nuclepore membrane filters and the colored dissolved
181 organic matter (CDOM) absorbance (A_{CDOM}) were obtained using a 1-cm path length quartz cuvette on a
182 Perkin Elmer Lambda-850 UV/VIS spectrophotometer equipped with an integrating sphere. The
183 Quantitative Filter Technique (QFT) with 0.7-µm GF/F filters were used to measure absorbance of
184 particles (A_{total}) and non-algal particles (A_{NAP}) inside an integrating sphere at 1 nm intervals from 300 to
185 800 nm. The absorption coefficients of CDOM (a_{CDOM}), NAP (a_{NAP}), particles (a_{total}) and phytoplankton
186 (a_{PHY}) were calculated using the following equations:

187
$$a_{CDOM}(\lambda) = 2.303 \times \frac{A_{CDOM}(\lambda)}{L} \qquad \ldots\ldots (1)$$

188 where L is the path length in meters. The a_{CDOM} were corrected for scattering, temperature, and baseline
189 drift by subtracting an average value of absorption between 700-750 nm for each spectrum (Joshi and
190 D'Sa, 2015).

191
$$a_{total}(\lambda) = 2.303 \times \frac{A_{total}(\lambda)}{V_{filtered}/S_{filter}} \qquad \ldots\ldots (2)$$

192
$$a_{NAP}(\lambda) = 2.303 \times \frac{A_{NAP}(\lambda)}{V_{filtered}/S_{filter}} \qquad \ldots\ldots (3)$$

193
$$a_{PHY}(\lambda) = a_{total} - a_{NAP} \qquad \ldots\ldots (4)$$

194 where $V_{filtered}$ is the filtered volume of sample, S_{filter} is the area of filter pads and the path length correction
195 for filter pad was applied according to (Stramski et al., 2015).

2.4 Pigment Absorption Spectra

197 The water samples were filtered with 0.7-µm GF/F filter. The filter pads were stored in liquid nitrogen
198 until transferred into 30 ml vials containing 10 ml cold 96% ethanol (Ritchie, 2006). The vials were spun
199 evenly to ensure full exposure of the filter pad to the ethanol and then kept in the refrigerator (in the dark)
200 overnight. The pigment solutions at room-temperature were poured off from vials into 1 cm cuvette and
201 measured on a Perkin Elmer Lambda-850 UV/VIS spectrophotometer to obtain pigment absorbance
202 spectra (A_{pig}), while, 90% ethanol was used as a blank (Thrane et al., 2015). The total absorption
203 coefficients of pigments $a_{pig}(\lambda)$ were calculated as follow:

204
$$a_{pig}(\lambda) = 2.303 \times \frac{A_{pig}(\lambda)}{L} \times \left(\frac{V_{ethanol}}{V_{filtered}}\right) \qquad \ldots\ldots (5)$$

205 where L is the path length in meters, $V_{ethanol}$ is the volume of ethanol, and $V_{filtered}$ is the filtered volume of
206 the water samples.

2.5 HPLC Measurements

208 Water samples were filtered through 0.7-µm GF/F filters and immediately frozen in liquid nitrogen for
209 HPLC analysis using the methods reported by Barlow et al. (1997). The detected pigments along with
210 their abbreviations are listed in Table 1. Diagnostic biomarker pigments are marked in bold letters (Table
211 1).

212 **Table 1**. Pigments information acquired from HPLC samples in Galveston Bay.

Variable	Primary Pigment (PPig)	Calculation
Chlorophylls		
[TChl a]	Total chlorophyll a (TChl a)	[Chlide a]+[DVChl a]+[Chl a]
[TChl b]	Total chlorophyll b (TChl b)	[DVChl b]+**[Chl b]**
[TChl c]	Total chlorophyll c (TChl c)	[Chl c$_1$]+[Chl c$_2$]+[Chl c$_3$]
Carotenoids		
[Caro]	Carotenes†	[ββ-Car]+[βε-Car]
[Allo]	**Alloxanthin**	
[Buta]	**19'-Butanoyloxyfucoxanthin**	
[Diadino]	Diadinoxanthin	
[Diato]	Diatoxanthin	
[Fuco]	**Fucoxanthin**	
[Hexa]	**19'-Hexanoyloxyfucoxanthin**	
[Peri]	**Peridinin**	
[Zea]	**Zeaxanthin**	
[Neo]	Neoxanthin	
[Lut]	Lutein	
[Viola]	Violaxanthin	
[Pras]	Prasinoxanthin	
[Anthera]	Antheraxanthin	

Note: (1) [Chl b], [Allo], [Fuco], [Peri], [Zea], [Buta] and [Hexa] are considered as diagnostic pigments for PFTs (Moisan et al., 2017).

Variable	Pigment Sum	Calculation
[TChl]	Total Chlorophyll (TChl)	[TChl a]+[TChl b]+[TChl c]
[PPC]	Photoprotective Carotenoids (PPC)	[Allo]+[Diadino]+[Diato]+[Zea]+[Caro]+[Viola]
[PSC]	Photosynthetic Carotenoids (PSC)	[Buta]+[Fuco]+[Hexa]+[Peri]+[Lut]+[Pras]
[PSP]	Photosynthetic Pigments (PSP)	[PSC]+[TChl]
[AP]	Total Accessory Pigments (AP)	[PPC]+[PSC]+[TChl b]+[TChl c]
[TP]	Total Pigments (TP)	[AP+[TChl a]
[DP]	Total Diagnostic Pigments (DP)	[PSC]+[Allo]+[Zea]+[T Chl b]

2.6 FIRe Measurements

214 An in-situ Fluorescence Induction and Relaxation System (FIRe, Satlantic Inc.) was used to characterize
215 phytoplankton photosynthetic physiology during the two surveys in GB. The FIRe is based on
216 illuminating a sample with an intense flash of light to instantaneously saturate the reaction centers of
217 photosystem II (PSII); under these light conditions, reaction centers do not accept electrons and most of
218 the absorbed light energy is dissipated as fluorescence. The fundamental parameter measured by FIRe is

219 fluorescence yield F(t), which is the emitted fluorescence divided by the irradiance intensity (no unit). In
220 contrast to strong flashes, dark adaption enables all reaction centers of PSII to be open with least
221 fluorescence emitted, thus, resulting in minimal fluorescence yield (F_o). Maximum fluorescence yield (F_m)
222 can be obtained after sufficient irradiation when all reaction centers are closed. Maximum photochemical
223 efficiency, which quantify the potential of converting light to chemical energy for the PSII reaction
224 centers (Moore et al., 2006), was calculated as (F_m - F_o)/ F_m = F_v / F_m. The functional absorption cross
225 section σ_{PSII} ($\text{Å}^2\text{quantum}^{-1}$) measures the capability of reaction centers to absorb light from the ambient
226 environment. The FIRe was deployed at a slow descent rate, with 12 and 20 vertical profiles obtained
227 during the first and second surveys, respectively. All measurements were programmed using standard
228 protocols of single saturating turn-over (ST) flash saturation of PSII (Kolber et al., 1998). Flashes were
229 generated from highly uniform blue LEDs at 455 nm with approximately 30 nm half-bandwidth. Chl a
230 fluorescence was stimulated using saturating sequence of 80 1.1 μs flashes applied at 1 μs intervals, 8
231 sequences were averaged per acquisition, and the fluorescence signal was detected at 668 nm. All data
232 were processed using standard FIReCom software (Satlantic). In addition, samples of 0.2-μm filtered sea
233 water at each station were used as 'blank' to remove the background fluorescence signals (Cullen and
234 Davis, 2003); in this step, the fluorescence from the filtered samples (without phytoplankton) were
235 subtracted from in-situ fluorescence signals to get more accurate values of F_v/F_m.

236 ## 2.7 Retrieving Phytoplankton Groups from above-water R_{rs}

237 A fundamental relationship that links sub-surface remote-sensing reflectance (r_{rs}) and the IOPs was
238 expressed using a quadratic function developed by (Gordon et al., 1988):

239
$$r_{rs} = g_1 * u(\lambda) + g_2 * u(\lambda)^2; \ u(\lambda) = \frac{b_b}{a_{total}+b_b} \qquad \ldots\ldots (6)$$

240 where, the parameters g_1 (~0.0788) and g_2 (~0.2379) are values for turbid estuarine waters (Joshi and
241 D'Sa, 2018); r_{rs} is the sub-surface remote sensing reflectance that were obtained from above-water remote
242 sensing reflectance (R_{rs}) using (Lee et al., 2002):

243
$$r_{rs} = \frac{R_{rs}}{0.52 + 1.7 \times R_{rs}} \qquad \ldots\ldots (7)$$

244 The total backscattering coefficient b_b is comprised of water (b_{bw}) and particulates including both organic
245 and inorganic particles (b_{bp}), while the total absorption coefficients (a_{total}) can be further separated into
246 four sub-constituents (Roesler and Perry, 1995) as indicated by:

247
$$b_b = b_{bw} + b_{bp}; \ a_{total} = a_w + a_{phy} + a_{CDOM} + a_{NAP} \qquad \ldots\ldots (8)$$

248 where a_w, a_{phy}, a_{CDOM}, and a_{NAP} represent the absorption coefficients of pure water, phytoplankton, colored
249 dissolved organic matter and non-algal particles, respectively.

250 The IOP inversion algorithm for retrieving IOPs from R_{rs} require known spectral shape (eigenvector) of
251 each component in Eq. (8) to estimate the magnitude (eigenvalues) of each component (Table 2). The
252 spectral shape can be adjusted by changing the values of slope based on characteristics of the study area.
253 It is worth noting that a single averaged phytoplankton eigenvector does not provide species information
254 whereas a set of several species-specific phytoplankton eigenvectors allow estimates of species
255 composition. IOPs inversion algorithm applied in this study makes use of mass-specific phytoplankton
256 absorption spectra of 10 groups namely, dinoflagellate, diatom, chlorophyte, cryptophyte, haptophyte,
257 prochlorophyte, raphidophyte, rhodophyte, red cyanobacteria and blue cyanobacteria; these were obtained

258 from Dierssen et al. (2006) and Dutkiewicz et al. (2015) as eigen vectors rather than using one average
259 $a_{phy}(\lambda)$ spectrum. Subsequently, the inversion algorithm iterates repeatedly to minimize the difference
260 between modeled R_{rs} and in-situ measured R_{rs} (R_{rs_insitu}) until a best fit is achieved while allowing for
261 alterations of all parameters listed in Table 2 (Chase et al., 2017). The absolute percent errors between
262 modeled and measured values of R_{rs}, a_{phy}, a_{CDOM}, a_{NAP} and b_{bp} were calculated as:

263
$$\%error = \left| \frac{X_{modeled} - X_{measured}}{X_{measured}} \right| \times 100 \qquad \qquad \ldots\ldots (9)$$

264 **Table 2.** Parameters and eigenvectors used in the semi-analytical inversion algorithm.

Parameter	Equation	Slope	Eigenvalue
$a_{CDOM}(\lambda)$	$a_{CDOM}(\lambda) = M_{CDOM} \times \exp^{-S_{CDOM} \times (\lambda - \lambda_0)}$; $\lambda_0 = 443$	S_{CDOM}	M_{CDOM}
$a_{NAP}(\lambda)$	$a_{NAP}(\lambda) = M_{NAP} \times \exp^{-S_{NAP} \times (\lambda - \lambda_0)}$; $\lambda_0 = 443$	S_{NAP}	M_{NAP}
$a_{phy}(\lambda)$	$a_{phy}(\lambda) = \sum Chl\ a_i \times a^*_{phi}$; a^*_{phi} is the spectral shape of each phytoplankton group.		$Chl\ a_i$
$b_{bp}(\lambda)$	$b_{bp}(\lambda) = B_{bp} \times (\lambda_0/\lambda)^{S_{bp}}$; $\lambda_0 = 443$	S_{bp}	B_{bp}
Note: $a^*_{phi}(\lambda)$ for 10 different groups of phytoplankton used in this study were extracted from (Dierssen et al., 2006) and Dutkiewicz et al., (2015).			

2.8 Retrieving Pigments from Sentinel 3-OLCI R_{rs}

2.8.1 Reconstruction of Pigment Absorption Spectrum by Multiple Linear Regression

267 Total pigment absorption spectra $a_{pig}(\lambda)$ obtained during both surveys (Eq. 5), were modeled as a third
268 order function of HPLC measured Chl a (Chl a_HPLC) concentration at each station as (Moisan et al., 2017):

269
$$a_{pig}(\lambda) = C_3 \times (Chl\ a\_HPLC)^3 + C_2 \times (Chl\ a\_HPLC)^2 + C_1 \times Chl\ a\_HPLC + C_0 \quad \ldots\ldots (11)$$

270 where vector coefficient C=[C_3, C_2, C_1, C_0], are wavelength-dependent coefficients that range from 400 to
271 700 nm at 1 nm interval; these were further applied to Sentinel-3A OLCI Chl a to calculate a_{pig_OLCI} at
272 each pixel as:

273
$$a_{pig\_OLCI}(\lambda) = C_3 \times (Chl\ a\_OLCI)^3 + C_2 \times (Chl\ a\_OLCI)^2 + C_1 \times Chl\ a\_OLCI + C_0 \quad \ldots\ldots (12)$$

274 where Chl a_OLCI is Sentinel-3A OLCI derived Chl a concentration (259×224 pixels); the obtained image
275 represents the value of a_{pig_OLCI} at a certain wavelength and 301 images of a_{pig_OLCI} can be obtained in
276 the 400-700 nm wavelength range at 1 nm interval.

2.8.2 Satellite Retrieval of Pigments using Non-Negative Least Square (NNLS) Inversion Model

278 The a_{pig_OLCI} is a mixture of n pigments with known absorption spectra $a_i(\lambda)$, $i = 1,2, \ldots, n$ at wavelength
279 λ (nm); thus, $a_{pig\_OLCI}(\lambda)$ can be considered as a weighted sum of individual component spectrum
280 (Thrane et al., 2015) at each image point as:

281

$$a_{pig\_OLCI}(\lambda) = x_1 \times a_1(\lambda) + x_2 \times a_2(\lambda) + \cdots x_n \times a_n(\lambda) \qquad \ldots\ldots (13)$$

282

283

284   where $A(\lambda) = [a_1(\lambda), a_2(\lambda), \ldots a_n(\lambda)]$ represent the mass-specific spectra of 16 pigments (Chl a, Chl b,
285   Chl c_1, Chl c_2, pheophytin-a, pheophytin-b, peridinin, fucoxanthin, neoxanthin, lutein, violaxanthin,
286   alloxanthin, diadinoxanthin, diatoxanthin, zeaxanthin, and β-carotenoid), which are the in-vitro pigment
287   absorption spectra over pigment concentrations and can be extracted from supplementary R scripts of
288   Thrane et al. (2015). The vector coefficient $X = [x_1, x_2, \ldots x_n]$ correspond to the concentrations (µg L^{-1}) of
289   these distinct pigments; note that X cannot be negative, therefore, non-negative least squares (NNLS) was
290   used to guarantee positive solutions of X (Moisan et al., 2013; Thrane et al., 2015). Eq. 13 can be further
291   expressed as:

292

$$\begin{bmatrix} a_{pig}(400)_{OLCI} \\ a_{pig}(401)_{OLCI} \\ \vdots \\ a_{pig}(700)_{OLCI} \end{bmatrix} = \begin{bmatrix} x_1 \\ x_2 \\ \vdots \\ x_n \end{bmatrix} \times \begin{bmatrix} a_1(400), a_2(400), \ldots a_n(400) \\ a_1(401), a_2(401), \ldots a_n(401) \\ \vdots \\ a_1(700), a_2(700), \ldots a_n(700) \end{bmatrix} \qquad \ldots\ldots (14)$$

293

2.9 Processing Approach

295   Sentinel 3A-OLCI pigment maps were generated using the processing pathway 1 (Fig. 2) that includes the
296   following: 1) developing empirical relationships between HPLC-measured Chl a and R_{rs_insitu} band ratio
297   for Sentinel 3A-OLCI band 9 (673 nm) and band 11 (709 nm) to generate Sentinel 3A-OLCI Chl a maps,
298   2) converting Chl a concentration to $a_{pig\_OLCI}(\lambda)$ maps, and subsequently decomposing $a_{pig\_OLCI}(\lambda)$ into
299   individual pigment spectra to generate phytoplankton pigment maps for GB. In processing pathway 2,
300   phytoplankton taxonomic composition at each sampling station was obtained from a 10-species IOP
301   inversion model, which take R_{rs_insitu} as input and estimates Chl a concentration of each phytoplankton
302   group (Fig. 2). Finally, CDOM-corrected FIRe measurements of F_v/F_m and σ_{PSII} were combined with
303   phytoplankton taxonomy to assess photosynthetic physiology of different phytoplankton groups.

304
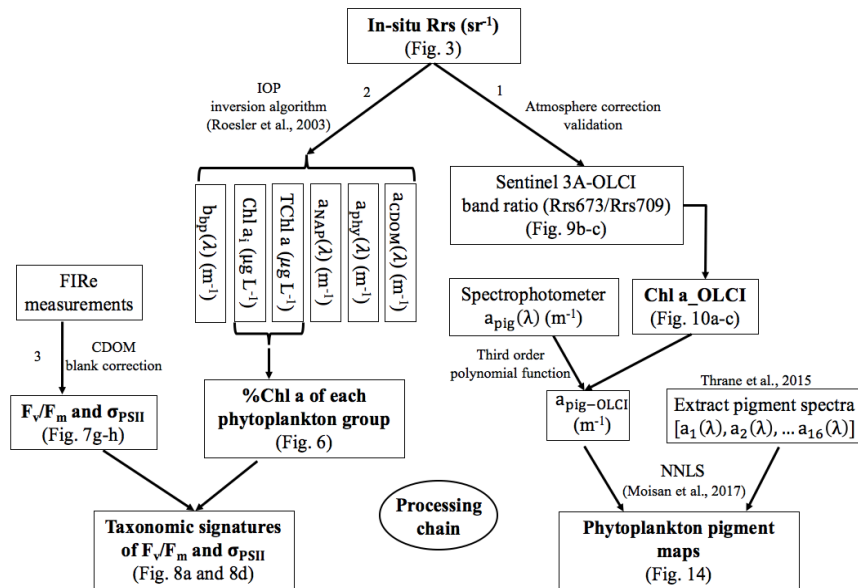
305   Figure 2. Flowchart showing the three processing steps for: (1) retrieving pigments spatial distribution
306   maps from OLCI, (2) distinguishing phytoplankton groups, and (3) assessing phytoplankton physiological

307   parameters and their linkages to taxonomic groups.

3. Results

3.1 Phytoplankton Taxonomy and Physiological State from Field Observations

3.1.1   Measurements of Above Water Remote Sensing Reflectance

311   Above-water remote sensing reflectances (R_{rs_insitu}) from the two surveys (Fig. 3) reflect the influence of
312   the absorbing and scattering features of water constituents. Low reflectance (~675 nm) caused by Chl a
313   red light absorption and maximum reflectance at green wavelength (~550 nm) were observed. Obvious
314   dips at ~625 nm versus reflectance peaks ~650 nm were observed in spectra during both surveys, which
315   could be attributed to cyanobacteria modulation of the spectra (Hu et al., 2010). The reflectance peak
316   around 690–700 nm was obvious at most sampling sites except at stations 13 and 14 adjacent to the
317   nGOM and were likely due to the effect of Chl a fluorescence (Gitelson, 1992; Gilerson et al., 2010). The
318   peak position at stations with lower Chl a concentration (~5 µg L^{-1}) were observed at 690-693 nm;
319   however, the peaks shifted to longer wavelengths of 705 and 710 nm for station 23 and 19 with extremely
320   high Chl a concentrations of ~31 and 50 µg L^{-1}, respectively (Fig. 3).
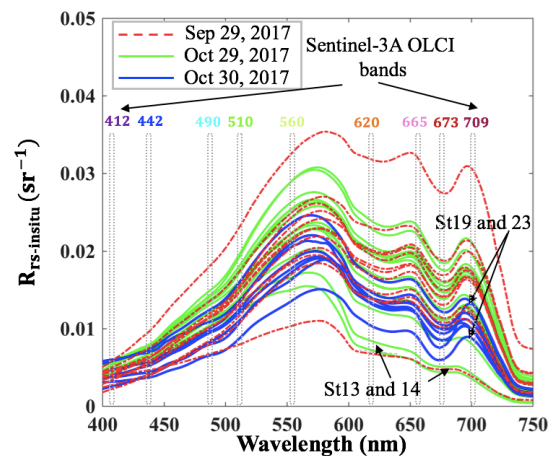
321
322   **Figure 3.** R_{rs_insitu} spectra at stations in GB on September 29, and October 29-30, 2017; vertical bars
323   represent Sentinel-3A OLCI spectral bands.

3.1.2   Performance of IOP Inversion Algorithm

325   The IOP inversion algorithm was applied to R_{rs_insitu} data (Fig. 3) obtained during the two surveys in GB.
326   The mean errors for modeled a_{CDOM}, a_{NAP}, a_{phy} and b_{bp_470} at all wavelengths for the 34 stations were
327   5.86%, 6.83%, 12.19% and 10.79%, respectively (Table 3). A total of 8 phytoplankton groups
328   (dinoflagellate, diatom, chlorophyte, cryptophyte, haptophyte, prochlorophyte, raphidophyte, and blue
329   cyanobacteria) were spectrally detected from IOP inversion algorithm. The sum of 8 eigenvalues of Chl_i
330   (Table 2) represents the modeled total Chl a (TChl $a_{\_mod}$) of the whole phytoplankton community. The
331   TChl $a_{\_mod}$ is better correlated with HPLC-measured total Chl a (TChl $a_{\_HPLC}$) for survey 2 (green circle;
332   Fig. 4a) with $R^2 \sim 0.92$, compared to survey 1 (red color; Fig. 4a). In addition, the TChl $a_{\_mod}$ appear to be
333   slightly higher than TChl $a_{\_HPLC}$ for survey 2. The modeled a_{CDOM} (a_{CDOM_mod}) are in close agreement with
334   spectrophotometrically measured a_{CDOM} at 412 nm (Fig. 4b), with a_{CDOM} obtained on September 29, 2017
335   much higher than that on October 29-30, 2017. The modeled b_{bp} (b_{bp_mod}) are well correlated with in-situ
336   b_{bp} (b_{bp_insitu}) at 470 nm (Fig. 4c) with higher R^2 (0.81) observed on September 29, 2017. In addition, both

337 modeled and field-measured b_{bp} showed stronger backscattering at most stations on September 29, 2017
338 than those on October 29-30, 2017.
339
340 **Table 3.** Error statistics over all wavelengths and sampling stations (N=301×34=10234; 12 and 22
341 stations on Sep 29 and Oct 29-30, 2017) from semi-analytical IOP inversion algorithm.
342

Parameter	Min. error (%)	Max. error (%)	Mean error (%)	R^2(Sep)	R^2(Oct)
R_{rs} $\lambda \in [400,700]$	0.005	40.12	18.71	0.90	0.89
$a_{CDOM}(\lambda)$, $\lambda \in [400,700]$	0.042	11.20	5.86	0.92	0.94
$a_{NAP}(\lambda)$, $\lambda \in [400,700]$	0.001	11.46	6.73	0.90	0.91
$a_{PHY}(\lambda)$, $\lambda \in [400,700]$	0.001	36.42	12.19	0.84	0.85
$b_{bp}(\lambda)$, $\lambda = 470$ nm	0.057	40.22	10.79	0.81	0.43

343
344 The Chl a percentage (%Chl a), which is Chl_i/TChl a, were also compared with diagnostic pigment
345 percentage (%DP), which is specific DP for each phytoplankton group over the sum of DP ($\sum DP$). The
346 DP for diatom (fucoxanthin), dinoflagellate (peridinin), cryptophytes (alloxanthin), chlorophyte (Chl b),
347 haptophyte (19'-hexanoyloxyfucoxanthin), and cyanobacteria (zeaxanthin) referred in (Moisan et al.,
348 2017) were used in this study. The R^2 between %Chl a and %DP for different phytoplankton groups range
349 from 0.15 to 0.81 (Fig. 4). The %Chl a of cryptophyte is between 5%-42% and well correlated with
350 alloxanthin/$\sum DP$ (R^2~0.62-0.72; Fig. 4d) for both surveys. In addition, the cryptophyte %Chl a at station
351 19 and 23 on October 30, 2017 was highest (~40%) in coincidence with the highest value of alloxanthin/
352 $\sum DP$ (Fig. 4d). Furthermore, relationship between chlorophyte %Chl a and Chl b/$\sum DP$ (R^2~0.55; Fig. 4e)
353 showed that chlorophyte during survey 1 contributed higher fraction to the whole phytoplankton
354 community compared to survey 2. The %Chl a of cyanobacteria highly correlated with zeaxanthin/$\sum DP$
355 with R^2 larger than 0.7 (Fig. 4f) for both surveys. Low %Chl a of dinoflagellate in coincidence with low
356 peridinin/$\sum DP$ (R^2~0.78) were observed at stations along the transect, however, increased contribution
357 of dinoflagellate appeared adjacent to the entrance during both surveys (Fig. 4g).

358
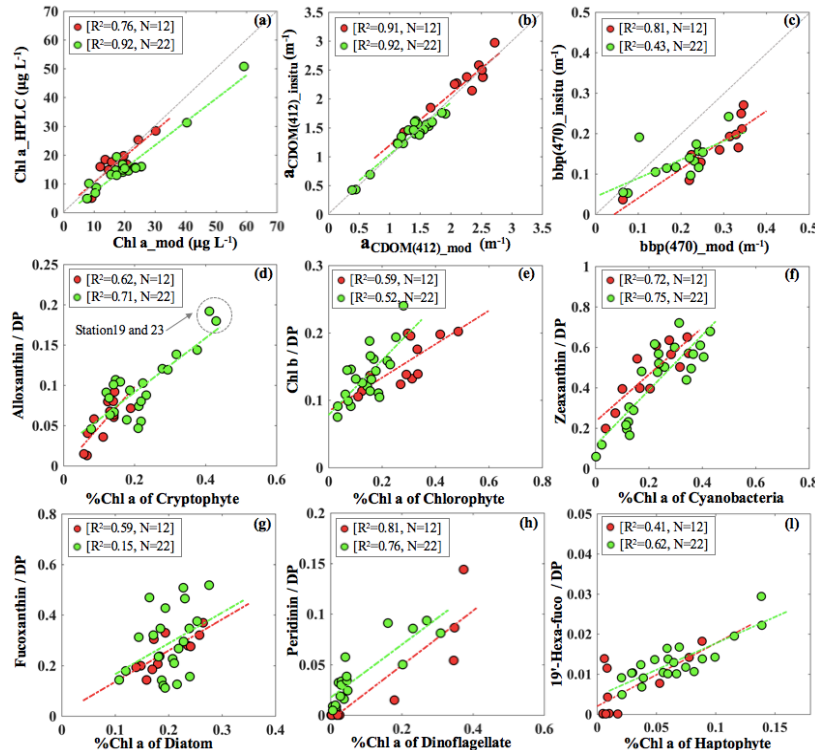
Figure 4. (a) Validation of TChl a_mod via HPLC-measured TChl a; individual %Chl a of each detected taxa versus corresponding %DP shown with (d) cryptophyte, (e) chlorophyte, (f) cyanobacteria, (g) diatom, (h) dinoflagellate, and (l) haptophyte; red and green dots indicate the samples on September 29 and October 29-30, 2017, respectively. Comparison between in-situ measurements and modeled results with (b) $a_{CDOM}(412)$ and (c) $b_{bp}(470)$.

3.1.3 Variations in Phytoplankton Community Structure

Reconstruction of the phytoplankton absorption coefficients spectra revealed variations in phytoplankton community structure (Fig. 5) even several weeks after Hurricane Harvey. The modeled a_{phy} spectra (a_{phy_mod}) at stations 6, 13, 17 and 19 (Fig. 5a-f) yielded spatiotemporal differences of phytoplankton taxonomic composition in GB. The strong absorption peak around 625 nm induced by cyanobacteria was observed at most of the stations for both modeled results and in-situ measurements (Fig. 5a, 5c and 5e) except at stations adjacent to the entrance (Fig. 5b and d). The a_{phy_mod} at station 6 was primarily dominated by group of cyanobacteria (blue line) and chlorophyte (green line) on September 29, 2017 (Fig. 5a); in contrast, the spectrum of chlorophyte contributed very little at station 6 on October 29, 2017 (green line; Fig. 5c). Furthermore, the shape of spectra for samples obtained at station 13 showed strong dinoflagellate-modulation versus extremely low cyanobacteria contribution during survey 1 (red line; Fig. 5b). However, small-size group like haptophyte and prochlorophyte displayed increasing proportions at station 13 on October 29, 2017 (Fig. 5d). Station 17 in the East Bay was dominated by cyanobacteria (blue line; Fig. 5e) and cryptophyte (pink line; Fig. 5e) absorption spectra, whereas, on October 30, 2017, the main spectral features at station 19 in the upper GB was from cryptophyte (pink line) and chlorophyte (green line; Fig. 5f).
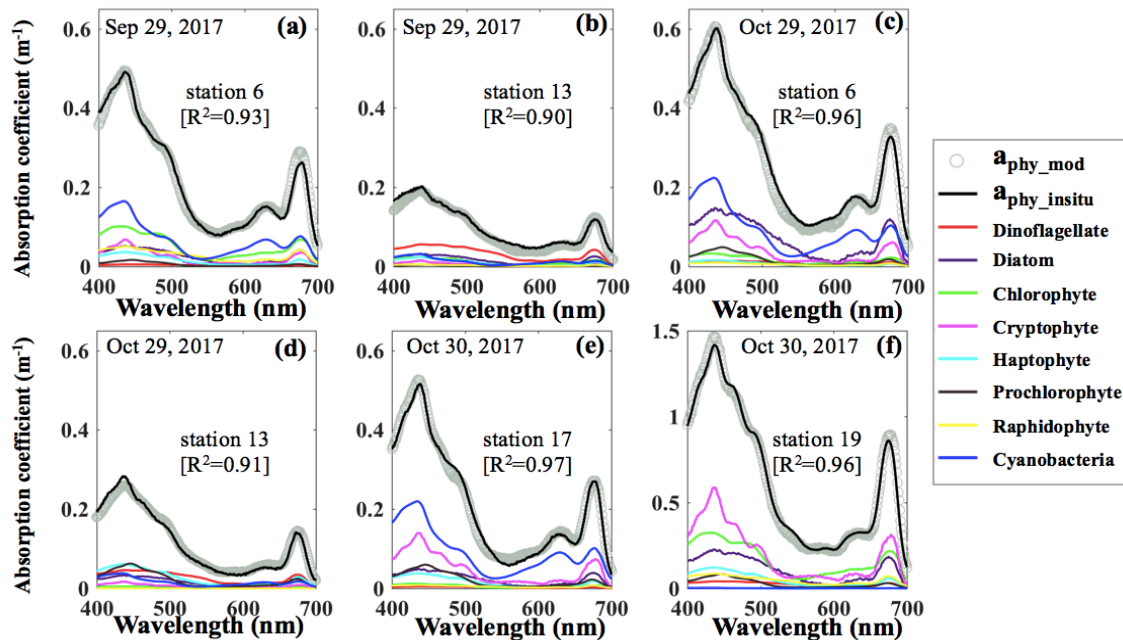
Figure 5. Reconstruction of phytoplankton absorption coefficients spectra at station 6 **(a)** and 13 **(b)** on September 29, 2017, at station 6 **(c)** and 13 **(d)** on October 29, 2017 and at 17**(e)**, and 19 **(f)** on October 30, 2017 based on the mass specific absorption spectra of different phytoplankton groups including diatom, chlorophyte, dinoflagellate, cryptophyte, cyanobacteria (blue), haptophyte, prochlorophyte and raphidophyte presented using different colors.

The corresponding taxa-specific %Chl a derived from IOPs inversion algorithm for the two surveys on September 29 and October 29-30, 2017 are shown in Figure 6a and 6b, respectively. Cyanobacteria (blue

389 bars) and chlorophyte (green bars) constituted over 55% of the phytoplankton communities during survey
390 1 (September 29, 2017; Fig. 6a). In addition, chlorophyte, known to proliferate in freshwater
391 environments, showed higher fraction than that observed in survey 2 (green color; Fig. 6). Further,
392 chlorophyte together with diatoms (purple color; Fig. 6a) accounted for ~ 60% of TChl a_mod at many
393 stations (e.g., station 7, 8 and 9) with a well-mixed water column (inferred from salinity profiles; not
394 shown) on September 29, 2017. Cryptophyte, haptophyte and raphidophyte became a minor component
395 of the community and accounted in total to ~25% of TChl a_mod (Fig. 6a). Furthermore, contribution by
396 dinoflagellate group to TChl a_mod was low inside the bay, but showed increasing %Chl a (~30%) in
397 higher salinity waters adjacent to the nGOM (red color; Fig. 6a). Cyanobacteria (blue color; Fig. 7)
398 exhibited a slightly elevated percentage during survey 2 (~60 days after hurricane passage, October 29-30,
399 2017) and were quite abundant at station 16, 17 and 18 in East Bay where the water was calm and
400 stratified as observed from salinity profiles. In addition, cyanobacteria were not prevailing adjacent to the
401 nGOM (Station 12, 13 and 14) and close to San Jacinto (station 19, 20, 21, 23 and 24), where cryptophyte
402 (pink color) and chlorophyte (green color) showed dominance (Fig. 6b). The %Chl a of chlorophyte
403 obtained at stations along the Trinity River transect decreased by ~10% on October 29-30, 2017
404 compared to that on September 29, 2017. Small size groups like haptophyte and prochlorophyte increased
405 on October 29-30, 2017 and were more abundant adjacent to the nGOM, accounting for more than 25%
406 of the TChl a_mod.
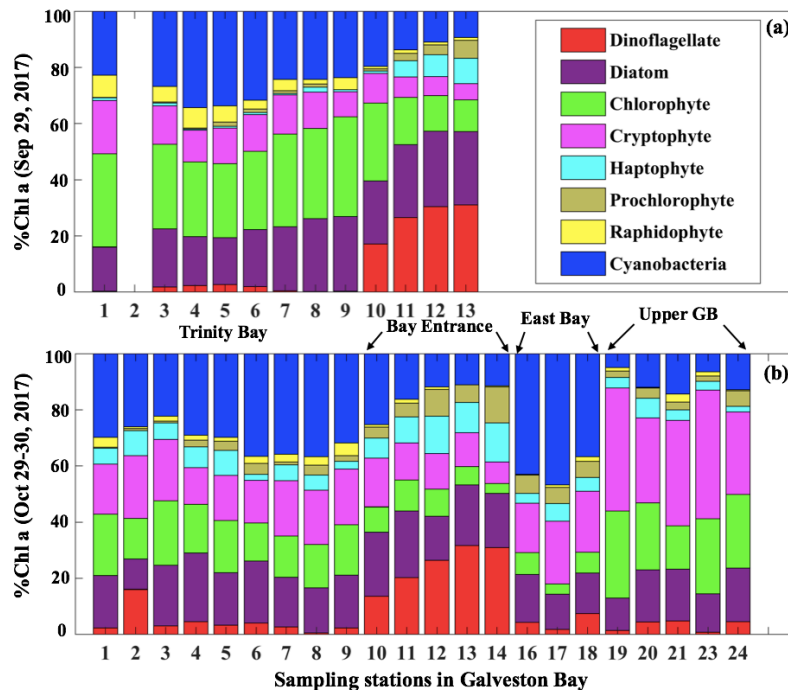
407
408 **Figure 6**. Phytoplankton taxonomic compositions detected from IOP inversion algorithm on September
409 29 and October 29-30, 2017 in Galveston Bay; phytoplankton groups are represented in different colors as
410 shown in the legend.

411 **3.1.4   Environmental Conditions and Physiological State of Phytoplankton Community**

412 The surface salinity presented a pronounced seaward increasing gradient along the transect (station 3-14)
413 during both the surveys (Fig. 7a) with primarily lower salinity throughout the bay during survey 1 in
414 comparison to survey 2, which indicated the freshening impact was still ongoing even 4 weeks after
415 Hurricane Harvey. The salinity was ~15 at station 16 and decreasing when going further into East Bay
416 (~10 at station 17 and 18; Fig. 7a). In upper GB, salinity at station 19-24 did not vary significantly (~15),
417 increasing along with the distance away from the San Jacinto River mouth with highest value (~17.5) at

418 station 24. During both surveys, lowest Chl a (Fig. 7b) were observed adjacent to the nGOM, and the
419 highest Chl a were closest to the river mouth. The photosynthetically Active Radiation (PAR) which were
420 calculated from down-welling irradiance (not shown here) decreased significantly with depth, but surface
421 PAR (Fig. 7c) were similar in magnitude at all stations. Pigment ratios including TChl a/TP (0.58-0.68),
422 PSC/Chl a (0.07-0.26) and AP/TP (0.34-0.42) were obtained from HPLC measurements and shown in
423 Figure 7d, 7e and 7f, respectively.

424 The CDOM calibrated and 0-0.5m depth averaged photosynthetic parameters F_V/F_M varied from 0.41 to
425 0.64 (Fig. 7g), while σ_{PSII} was in the range of 329-668 $Å^2$quantum^{-1}(Fig. 7h). The highest σ_{PSII} and
426 lowest F_V/F_M appeared adjacent to the nGOM (station 12-14). Conversely, values of F_V/F_M at stations 7-9
427 with a well-mixed water column were high with low values of σ_{PSII}. Both F_V/F_M and σ_{PSII} did not
428 directly correlate with Chl a, (e.g., high Chl a ~51 µg L^{-1} at station 19 corresponded to a relatively low
429 level of F_V/F_M ~0.45, versus high σ_{PSII} ~550 $Å^2$quantum^{-1}). However, the stations with high F_V/F_M
430 coincided with the high fraction of Chl a (Chl a/TP) and low fraction of AP (AP/TP) (Fig. 7d and 7f). In
431 contrast, σ_{PSII} showed an overall positive relationship with AP/TP, but altered negatively with Chl a/TP
432 during both surveys. The lowest (highest) value of σ_{PSII} (F_V/F_M) were observed at station 9 corresponding
433 to the highest Chl a/TP value (~0.64) on October 29, 2017. The highest AP/TP and PSC/Chl a were
434 obtained from stations adjacent to the nGOM.

435
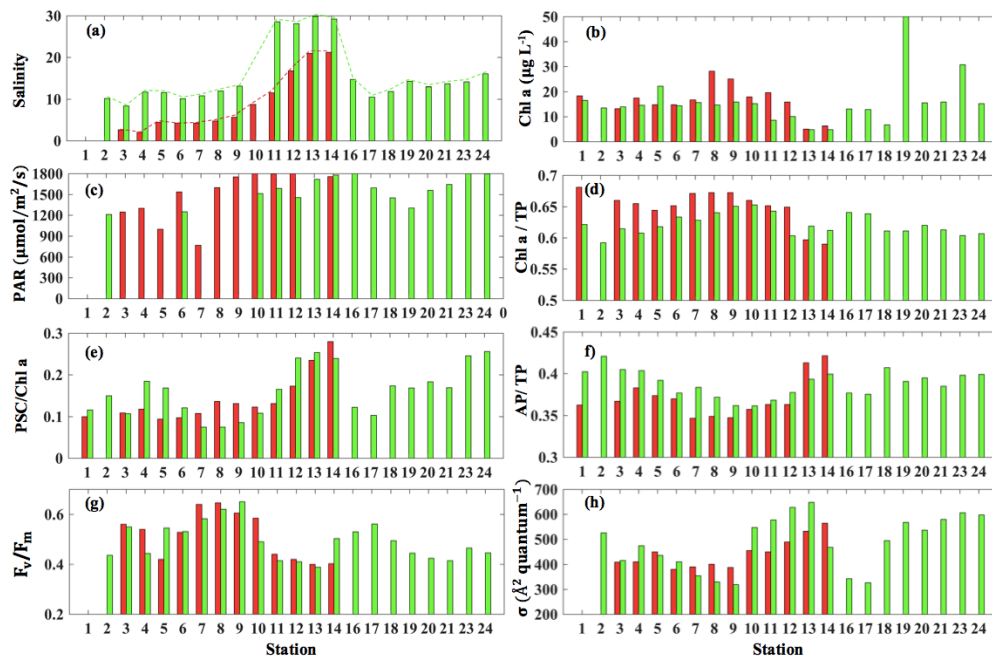
436 **Figure 7**. Environmental conditions (salinity, light field), pigment composition and physiological state in
437 GB surface waters (red bars indicating samples from September 29, 2017 and blue bars representing
438 samples from October 29 and 30, 2017). **(a)** Salinity, **(b)** Chl-a concentration, **(c)** PAR, **(d)** Chl a/TP, **(e)**
439 PSC/Chl a, **(f)** AP/TP, **(g)** F_V/F_m, and **(h)** σ_{PSII}.

440 **3.1.5 F_v/F_m and σ_{PSII} Taxonomic Signatures**

441 Distinct pigments housed within phytoplankton light-harvesting antennae can strongly influence PSII
442 light-harvesting capability and the photosynthetic quantum efficiency of phytoplankton (Lutz et al., 2001).
443 In this study, we observed an inverse relationship (R^2~0.63-0.81; Fig. 8a and d) between the F_V/F_M and

444 σ_{PSII}, that appeared related to taxonomic signals during surveys 1 and 2 in GB. Stations 1-9 along the
445 transect were considered as well-mixed group with no dominance by any particular group (black circles;
446 Fig. 8a-c); stations 10-14 close to the entrance were however, strongly dominated by dinoflagellate and
447 haptophyte (red symbol; Fig. 8a-c) during survey 1. This well-mixed group displayed low values of σ_{PSII}
448 (~390-439 Å^{2}quantum^{-1}), and high levels of F_V/F_M (~0.42-0.65) with F_V/F_M approaching 0.65 at station
449 9 on September 29, 2017 (Fig. 8a). However, enhanced contributions of dinoflagellate and haptophyte
450 around the entrance corresponded to a decline of F_V/F_M (0.3~0.4) against an increase of σ_{PSII} (500~600
451 Å^{2}quantum^{-1}) during survey 1. Furthermore, samples obtained from survey 2 at station 1-9, station 10-
452 14, station 16-18 and station 19-24 were considered as well-mixed (black), dinoflagellate-haptophyte
453 dominated (red), cyanobacteria dominated (blue) and cryptophyte-chlorophyte dominated (green),
454 respectively. Stations 16-17 dominated by cyanobacteria (blue triangles; Fig. 8d) showed high level of
455 F_V/F_M (0.5~0.6) and relatively low values of σ_{PSII} (300~400 Å^{2}quantum^{-1}). The F_v/F_m and σ_{PSII} of
456 cryptophyte-chlorophyte dominated stations showed a moderate level of F_V/F_M (0.4~0.5) and σ_{PSII}
457 (580~680 Å^{2}quantum^{-1}). More importantly, tight positive relationships existed between measurements
458 of F_V/F_M and Chl a/TP (R^2~0.31-0.63; Fig. 8b and e). On the other hand, σ_{PSII} were positively correlated
459 with PSC/Chl a with R^2~0.6 (Fig. 8c and f). The PSC/Chl a of cyanobacteria dominated group (blue
460 symbols), and well mixed group (brown symbols) were relatively low. Highest PSC/Chl a and lowest Chl
461 a/TP was observed for the dinoflagellate-haptophyte dominated group, corresponding to the lowest σ_{PSII}
462 and highest F_V/F_M. In addition, cryptophyte-chlorophyte dominated group had high levels of PSC/TChl a
463 (~0.18-0.26) and slightly higher Chl a/TP compared to dinoflagellate-haptophyte dominated group.
464 Overall, well-mixed groups with high proportion of large-size phytoplankton (e.g., diatoms and
465 chlorophyte) showed higher Chl a/TP along with larger F_V/F_M and smaller σ_{PSII} than those stations with
466 high fraction of dinoflagellate and pico-populations (Fig. 8c and f).
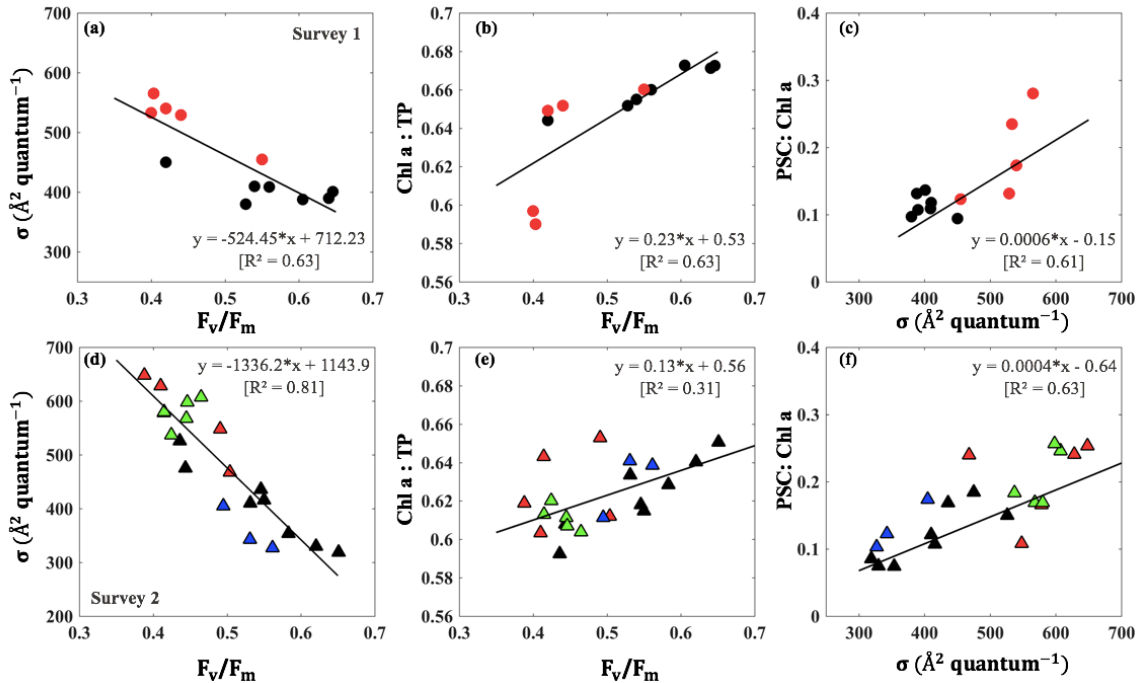
467
468 **Figure 8**. **a**, **d)** σ_{PSII} against F_V/F_M; **b**, **e)** F_V/F_M versus Chl a/TP; and **c**, **f)** σ_{PSII} versus PSC/Chl a on
469 September 29 and October 29-30, 2017 respectively. The data points identified by dominant taxa with
470 black, red, green and blue symbols denoting well-mixed, dinoflagellate-haptophyte dominated,
471 cryptophyte-chlorophyte dominated, and cyanobacteria dominated groups, respectively.

472 **3.2 Satellite Observations of Phytoplankton Pigments**

3.2.1 An OLCI Chl a Algorithm and its Validation

Blue to green band ratio algorithms have been widely used to study Chl a in the open ocean and shelf waters (D'Sa et al., 2006; Blondeau-Patissier et al., 2014); however, these bands generally fail in estuarine waters due to strong blue absorption by the high levels of CDOM and suspended particulate matter, especially after flooding events associated with hurricanes (D'Sa et al., 2011; D'Sa et al., 2018; Joshi and D'Sa, 2018). The percentage contribution by CDOM fluorescence (blank) to maximum fluorescence yield (F_m) obtained from in-situ FIRe (Fig. 9a) demonstrated that Chl a fluorescence was strongly influenced by high amounts of CDOM fluorescence in GB, especially during the first survey (September 29, 2017), when the bay was under strong floodwater influence (red triangles; Fig. 9a). The CDOM fluorescence signal constituted ~ 25 % in the region adjacent to the nGOM (stations 12-14), between 25%-50% in the upper GB, and up to ~65% in Trinity Bay, which implied that blue and even green band are highly contaminated by CDOM and might not be the most suitable bands for estimating Chl a in GB. However, an increase in peak height near 700 nm and its shift towards longer wavelength (Fig. 3) can be used as a proxy to estimate Chl a concentration (Gitelson, 1992).
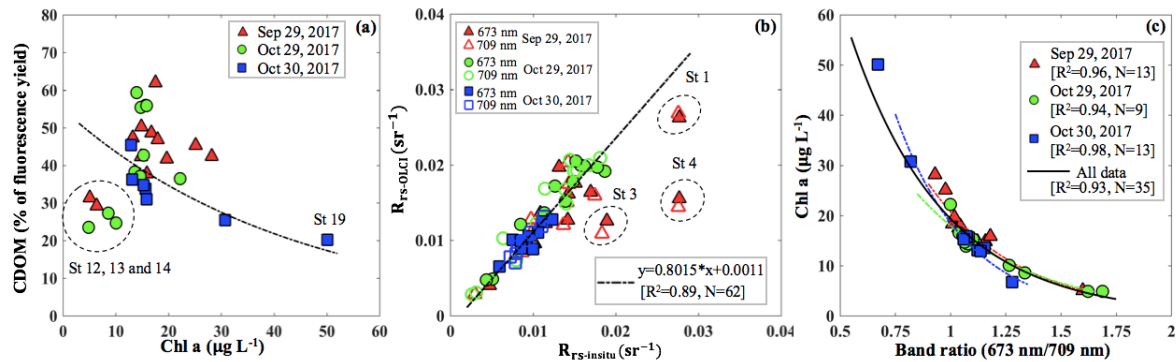
Figure 9. (a) Relationship between the percentage of the fluorescence yield of CDOM measured by FIRe against HPLC measured Chl a concentration. **(b)** Comparisons between R_{rs_insitu} and R_{rs_OLCI} at band 9 (673 nm) and band 11 (709 nm). **(c)** Exponential relationships between HPLC-measured Chl a concentrations and R_{rs_insitu} band ratio (673 nm/709 nm) in GB on September 29 (R^2=0.89), October 29 (R^2=0.93) and October 30 (R^2=0.97). Red, green and blue lines and symbols indicate data sets obtained on September 29, October 29 and 30, 2017 respectively.

The C2RCC atmospheric-corrected R_{rs_OLCI} at each of the sampling sites were further compared with R_{rs_insitu} (Fig. 3) at phytoplankton red absorption (~673 nm) and Chl a fluorescence (~700 nm) bands (Fig. 9b). The C2RCC performed overall better for the second survey on October 29-30, 2017 (green and blue symbols; Fig. 9b) than the first survey on September 29, 2017 (red triangles; Fig. 9b) when stations 1, 3 and 4 (circled triangles; Fig. 3c) adjacent to the Trinity River mouth were included; these stations were the last sampling sites in the afternoon (~4:30 pm) and under somewhat cloudy conditions. The time difference between satellite pass and in-situ measurements, sky conditions and shallow water depth also likely introduced more errors at these locations. The R^2 between R_{rs_OLCI} and R_{rs_insitu} at red and near infrared (NIR) bands was 0.89 when the data from station 3 and 4 were excluded, suggesting good usability of these two bands for Chl a empirical algorithms in GB. Thus, the higher the Chl a concentration, the stronger the red light absorption, resulting in higher reflectance at 709 nm; consequently, negative correlations were observed between Red/NIR band ratio and Chl a. The ratio of Red (~673 nm) and NIR (709 nm) reflectance bands from in-situ measurements were overall highly correlated with HPLC-measured Chl a with R^2 ~ 0.96, 0.94 and 0.98 on September 29, October 29 and

508 October 30, 2017, respectively (Fig. 9c). The Sentinel-3A OLCI Chl a maps (Fig. 10a-c) were generated
509 for all data based on the relationship between Chl a and the Red and NIR band ratio as:

$$\text{Chl a } (\mu g\ L^{-1}) = 216.38 \times \exp\left(-2.399 \times \frac{R_{rs}\ (673)}{R_{rs}\ (709)}\right) \quad \text{[All data]} \qquad \text{......} \ (15)$$

511 The OLCI-derived Chl a (Fig. 10a-c) showed a good spatial agreement with Chl a_HPLC (Fig. 10d-f). In
512 addition, a comparison of this algorithm with that of Gilerson et al., 2010 revealed slightly better
513 performance (not shown) inside of GB and especially in the area adjacent to the shelf.

514
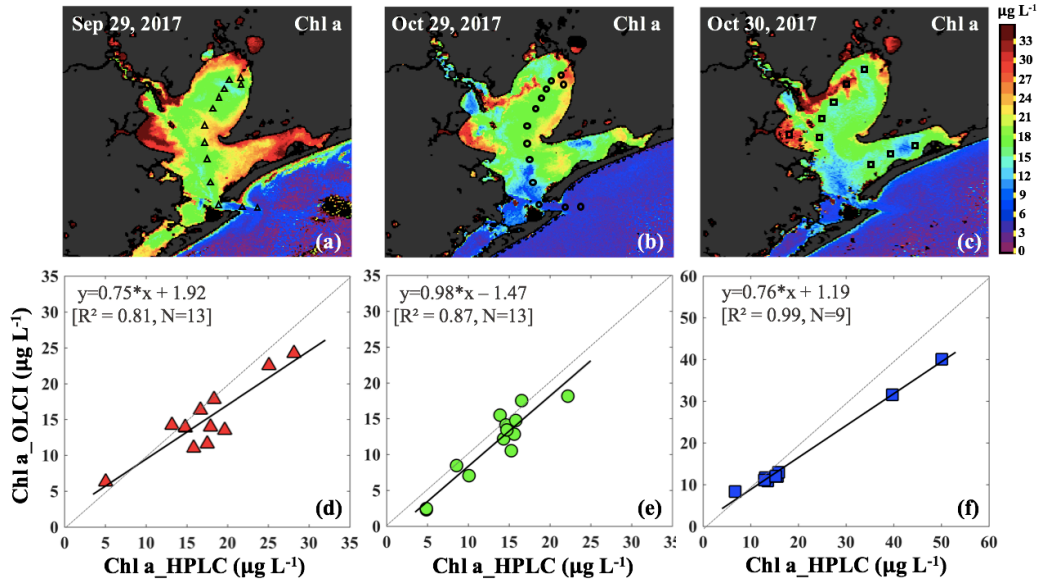
515 **Figure 10**. Chl a concentration generated based on in-situ band ratio ($R_{rs}673/R_{rs}709$) algorithm with (a),
516 (b) and (c) representing Chl a distribution on September 29, October 29 and October 30, 2017,
517 respectively; (c), (d) and (f) show the validation between HPLC-measured Chl a and OLCI-derived Chl a
518 on September 29, October 29 and October 30, 2017, respectively.

519 The Chl a concentration on September 29, 2017 was overall higher than that on October 29-30, 2017
520 through the entire bay. East Bay displayed very high Chl a concentration, with highest value (>30 $\mu g\ L^{-1}$)
521 observed on September 29, 2017 (Fig. 10a). The narrow shape and shallow topography of East Bay
522 results in relatively higher water residence time (Rayson et al. 2016); thus, the reduced exchange with
523 shelf waters likely lends the East Bay vulnerable to eutrophication. The average Chl a concentration on
524 October 29-30, 2017 were ~ 15 $\mu g\ L^{-1}$ along the transect (station 1-11) and ~4-6 $\mu g/L$ (station 12-14)
525 close the entrance of GB. In addition, Chl a adjacent to San Jacinto River mouth (>16 $\mu g\ L^{-1}$) was higher
526 than that in Trinity Bay, which might suggest that San Jacinto inflow had higher nutrient concentrations
527 than Trinity as also previously reported (Quigg et al., 2010). Furthermore, the OLCI-Chl a maps on
528 October 29 and 30, 2017 showed extremely high Chl a concentration in a narrow area adjacent to the San
529 Jacinto River mouth, with Chl a approaching ~ 40 $\mu g\ L^{-1}$ at station 19 (Fig. 10c).

530 **3.2.2   Long-term Chl a Observations in Comparison with Hurricane Harvey Event**

531 OLCI-derived Chl a maps between August, 2016-November, 2017 (Fig. 11a₁-a₁₅) and time series of
532 averaged Chl a values in the areas of Trinity Bay, East Bay and adjacent to the nGOM (Fig 11b) revealed
533 regionally different responses of Chl a to freshwater discharge from the San Jacinto and the Trinity Rivers
534 (Fig. 11b). Due to the relatively much higher discharge from the Trinity River, the spatial distribution of
535 Chl a in the bay (Fig. 11) generally indicates its greater influence than the San Jacinto River. During the

536   winter, and spring in 2017, phytoplankton Chl a peaks ~32 µgL^{-1} in Trinity Bay (Fig. 11b) were observed
537   after high inflows from both rivers (Fig. 11a$_5$-a$_8$). Chla then slightly decreased to ~20 µgL^{-1} in summer
538   (July and August, 2017). Generally, Chl a showed overall lower value (~10 µgL^{-1}) between September-
539   December, 2016 compared to 2017 in the absence of meteorological and hydrological events (Fig. 11a$_1$-
540   a$_4$). However, with the East Bay less directly affected by river discharge, Chl a levels remained fairly
541   constant in the range of ~18-24 µgL^{-1} before hurricane. In contrast, extremely high river discharge (~3300
542   m^{3}s^{-1}) induced by Hurricane Harvey in late August, 2017, elevated Chla in both Trinity and East Bay to
543   higher levels as observed on September 14, 2017 (~30-35 µgL^{-1}; Fig. 11a$_{11}$) compared to mean state of
544   fall season in 2016. Chl a then continuously decreased through September to October, 2017 in Trinity and
545   East Bay and were relatively low (≤10 µgL^{-1}) in November, 2017 under no additional pulses of river
546   discharge. Concentration of Chla adjacent to the entrance of GB exhibiting much lower values year round
547   than that of the Trinity and East Bay, and also showed slight positive responses to the enhanced river
548   discharge and the hurricane-induced flooding events. In addition, Chl a concentrations always displayed
549   low values along the Houston Ship Channel.

550
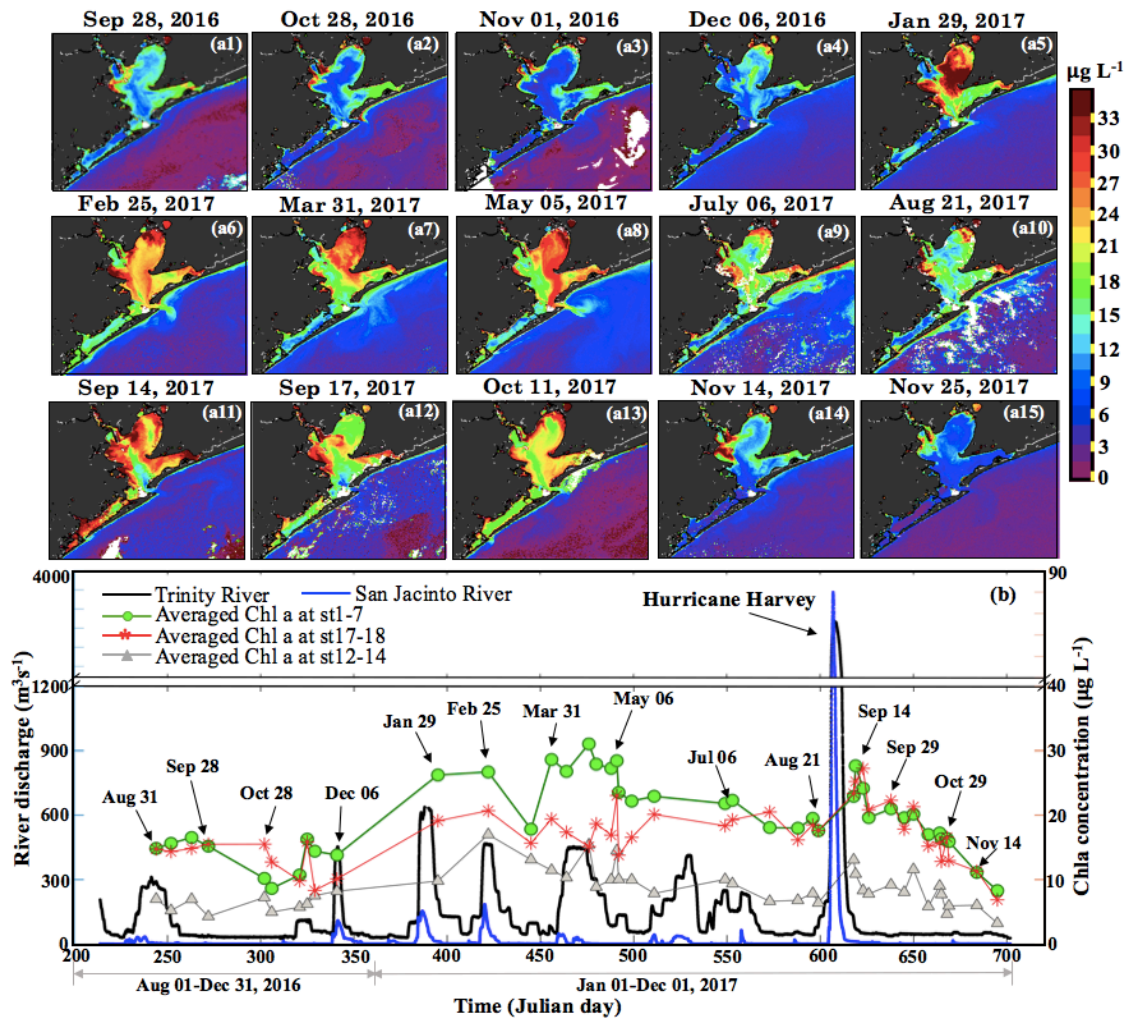
551   **Figure 11**. (**a$_{1-15}$**) OLCI-derived Chl a shown for the period of August 31, 2016-November 25, 2017. (**b**)
552   Trinity River discharge at Romayor, Texas (USGS 08066500, black line) and the west flank of the San
553   Jacinto River (USGS 08067650; blue line); the green, red and gray lines/symbols represent the mean of
554   Chl a at stations 1-7 in Trinity Bay, at stations 17-18 in East Bay and at stations 12-14 close to the

555   entrance of GB corresponding to 43 cloud free Sentinel 3A-OLCI images (colored symbols; dated
556   symbols correspond to images **a$_{1-15}$**).

3.2.3   Reconstruction of Total Pigment Absorption Spectra from OLCI-derived Chl a

558   The reconstructed $a_{pig}(\lambda)$ based on the third order function of Chl a$_{HPLC}$ (gray lines; Fig. 12a and b)
559   agreed well with the spectrophotometrically measured $a_{pig}(\lambda)$ (black lines; Fig. 12a and b) during both
560   surveys (R^2=0.86; Fig. 12c). The R^2 for modeled versus measured $a_{pig}(\lambda)$ are between 0.76 and 1.00 from
561   400 to 700 nm with averaged R^2 of whole spectra reaching ~ 0.82 on September 29, 2017 and ~0.89 on
562   October 29-30, 2017, respectively. The vector coefficients $C = [C_3, C_2, C_1, C_0]$ obtained from Eq. (11)
563   were further applied to Eq. (12) to generate $a_{pig\_OLCI}(\lambda)$ based on OLCI-derived Chl a images on July 06
564   (Fig. 11a$_9$), September 29 (Fig. 10a), October 29-30 (Fig. 10b-c), and Nov 25 (Fig. 11a$_{15}$), 2017,
565   respectively; these contained 259×224 pixels in each image. The $a_{pig\_OLCI}(\lambda)$ at each pixel was retrieved
566   at 1 nm interval, and thus 301 images of $a_{pig\_OLCI}(\lambda)$ representing each wavelength were obtained over GB.

567
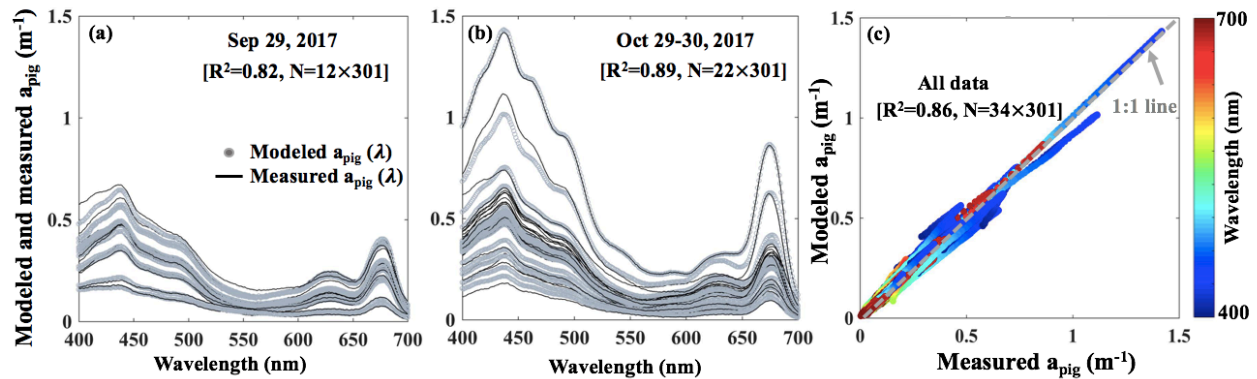
568   **Figure 12**. Spectrophotometrically measured and multi-regression fitted $a_{pig}(\lambda)$ spectra acquired on **(a)**
569   September 29 and **(b)** October 29-30, 2017 in GB. Gray and black lines represent modeled and measured
570   results, respectively. **(c)** Comparison between modeled and spectrophotometrically measured $a_{pig}(\lambda)$ for
571   all data with color representing wavelength.

3.2.4   Accuracy of phytoplankton pigment retrievals from Sentinel 3A-OLCI

573   The reconstructed $a_{pig\_OLCI}(\lambda)$ was spectrally decomposed into 16 individual pigment spectra at each pixel
574   based on Eq. (14). A comparison of all data between HPLC-measured pigments and NNLS algorithm
575   inverted pigments showed that R^2 ranged from a low of 0.40 for diatoxanthin to 0.96 for Chl a and RMSE
576   was in the range of 0.103-0.584 (Table 4). The NNLS-modeled Chl a also correlated well with OLCI-
577   derived Chl a (R^2=0.98; Fig. 13a), with each exhibiting similar quantitative and spatial patterns. For the
578   other 15 simultaneously simulated pigments, R^2 of only 7 pigments were greater than 0.650 (Table 4). In
579   addition, the produced RMSE were less than 0.3 for most of pigments, except zeaxanthin, violaxanthin,
580   diatoxanthin and diadinoxanthin. Further, those pigments with relatively lower RMSE, their slopes were
581   very close to 1 and y-intercepts approached to 0. Five NNLS-derived versus HPLC measured diagnostic
582   pigments including alloxanthin, Chl b, zeaxanthin, fucoxanthin and peridinin are shown in Figure 13. The
583   R^2 between NNLS-derived and HPLC-measured pigments for surveys 1 and 2 was highest for alloxanthin
584   (0.91; Fig. 13b). For the other pigments R^2 was 0.854 for Chl b (Fig. 13c), 0.689 for zeaxanthin (Fig.
585   13d), 0.645 for fucoxanthin (Fig. 13e) and 0.566 for peridinin (Fig. 13f), respectively.

586   **Table 4**. Correlation between HPLC-measured pigment concentration with NNLS-modeled pigments.

Pigment	R^2	slope	intercept	RMSE
Chl a	0.963	0.878	0.099	0.125
Chl b	0.854	0.791	0.091	0.214
Chl c_1	0.701	0.842	0.112	0.199
Chl c_2	0.626	0.884	0.134	0.103
Pheophythin a	0.812	0.841	0.097	0.114
Pheophythin b	0.783	0.632	0.112	0.145
Peridinin	0.566	0.649	0.081	0.246
Fucoxanthin	0.625	0.651	0.383	0.189
Neoxanthin	0.691	0.627	0.142	0.279
Lutein	0.742	0.651	0.109	0.298
Violaxanthin	0.426	0.456	0.415	0.389
Alloxanthin	0.912	0.592	0.107	0.227
Diadinoxanthin	0.512	0.446	0.721	0.396
Diatoxanthin	0.401	0.423	0.693	0.423
Zeaxanthin	0.689	0.516	0.802	0.584
B-carotenoid	0.648	0.469	0.216	0.241

587
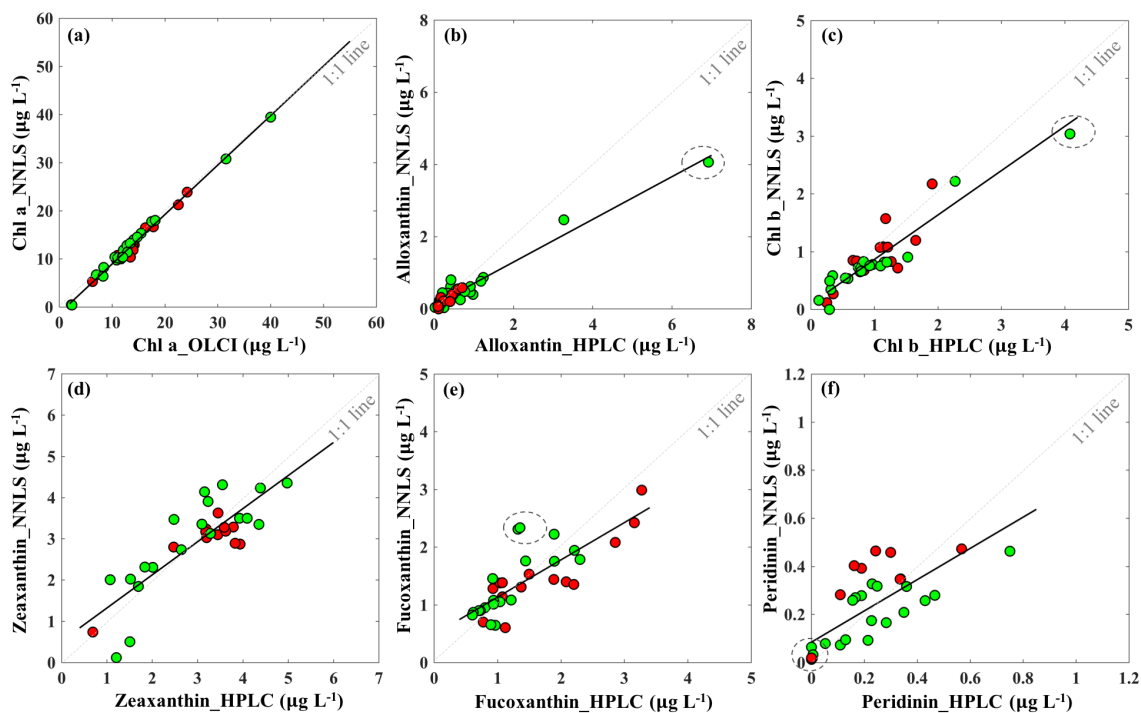
Figure 13. Sentinel-3A OLCI derived pigment concentration against HPLC measured pigment concentration in Galveston Bay; **a)** Chl a, **b)** alloxanthin, **c)** Chl-b, **d)** zeaxanthin, **e)** fucoxanthin, and **f)** peridinin. Red and green symbols indicate data sets obtained on September 29, and October 29-30, 2017 respectively.

3.3.1   Spatiotemporal Variations of Diagnostic Pigments

Flooding due to Hurricane Harvey not only enhanced Chl a, but also affected the phytoplankton pigments composition. NNLS-retrieved pigment maps for July, September, October, and November, 2017 including those of alloxanthin, chl b, zeaxanthin, fucoxanthin and peridinin (Fig. 14) showed different levels of variations before and after the hurricane event. Alloxanthin, which is unique to cryptophytes

597 (Wright and Jeffrey, 2006) exhibited same spatial distribution patterns (Fig. 14a_1-e_1) with Chl a.
598 Alloxanthin was especially low (~ 0.5 µg L^{-1}, Fig. 14a_1) in the major basin area on July 06, 2017 before
599 the hurricane and slightly elevated (~0.7 µg L^{-1}, Fig. 14b_1) in September and October, 2017 after the
600 hurricane passage. Furthermore, extremely high alloxanthin (~ 3.5 µg L^{-1}, Fig. 14c_1-d_1) was observed
601 adjacent to San Jacinto River mouth on October 29-30, 2017, which coincided with the high %Chl a of
602 cryptophyte at stations 19 and 23 (Fig. 6b). The bloom with high concentration of alloxanthin on October
603 29, 2017 (~3.5 µg L^{-1}; Fig. 14c_1) then extended to a broader area on October 30, 2017 (Fig. 14d_1).

604

605 Chl b is abundant in the group of chlorophyte (green algae) (Hirata et al., 2011) and the spatial
606 distributions of Chl b (Fig. 14a_2-e_2) also showed strong correlations with Chl a on July 06, 2017,
607 September 29, October 29-30 and November 25, 2017. The NNLS-derived Chl b exhibited overall low
608 values (~0.5-2 µg L^{-1}; Fig. 14a_2) before the hurricane and showed obvious elevation throughout the bay
609 after the hurricane and eventually decreasing to pre-hurricane level by November 25, 2017. Furthermore,
610 Chl b concentrations observed on September 29, 2017 were higher than that on October 29-30, 2017,
611 which corresponded to a decline of chlorophyte percentage derived from the IOP inversion algorithm (Fig.
612 6). More importantly, images obtained from IFCB at the entrance to GB also detected freshwater species
613 Chlorophyte (*Pediastrum duplex;* Fig. 14g) on September 29, 2017. However, this species was rarely
614 observed in IFCB images for the other dates (Fig. 14a_1 and Fig. 14c_1-e_2). In addition, Chl b concentrations
615 approached ~2.8 µg L^{-1} in the bloom area and the corresponding green discoloration of water was also
616 observed during the field survey on October 30, 2017.

617 Zeaxanthin is known as taxa-specific pigment for prokaryotes (cyanobacteria) (Moisan et al., 2017;
618 Dorado et al., 2015) and NNLS-derived zeaxanthin maps (Fig. 14a_3-e_3) displayed significantly different
619 patterns with Chl a, exhibiting low concentrations in the areas where the Chl a were high. For example,
620 zeaxanthin was especially low in the bloom area on October 29-30, 2017, which agreed well with
621 low %Chl a of cyanobacteria at stations 19 and 23 (Fig. 6), thus indicating that this localized algal bloom
622 event was not associated with cyanobacteria. In addition, zeaxanthin was high ~ 3.0 µg L^{-1} (Fig. 14a_3) in
623 both GB and shelf waters on July 06, 2017 before the hurricane event. Later, zeaxanthin increased a
624 slightly on September 29, 2017 (Fig. 14b_3) with IFCB data detecting N$_2$-fixing cyanobacteria (*Anabaena*
625 spp.; Fig. 14g) and remained elevated on October 29-30, 2017 (Fig. 14b_3-c_3). Zeaxanthin eventually
626 decreased to very low values (~ 1.2 µg L^{-1}; Fig. 14e_3) on November 25, 2017.

627 Fucoxanthin is a major carotenoid found in diatoms (Hirata et al., 2011; Moisan et al. 2017) and the
628 NNLS-derived fucoxanthin maps (Fig. 14a_4-e_4) showed highly similar distribution patterns with Chl a.
629 Maps of fucoxanthin showed low concentrations on July 06, 2017 (~1.5 µg L^{-1}; Fig. 11a_4), and displayed
630 a large increase on September 29, 2017 (~1.6-3.0 µg L^{-1}; Fig. 11b_4). Diatom group detected from IFCB
631 were dominated by marine species before the hurricane, but subsequently shifted to freshwater species
632 (e.g., *Pleurosigma*; Fig. 14g) and then back to marine species after October, 2017. Overall, fucoxanthin
633 concentrations in GB were relatively higher during survey 1, which corresponded to the higher %Chl a of
634 diatom (Fig. 6) compared to survey 2. Although, fucoxanthin decreased to low values on November 25,
635 2017 (~1.6 µg L^{-1}; Fig. 11e_4), it accounted for higher fraction of phytoplankton diagnostic pigments
636 compared to other dates in July, September and October, 2017.

637

638 Peridinin, a primary bio-marker pigment for certain dinoflagellates (Örnólfsdóttir et al., 2003), also
639 displayed significantly distinct patterns in comparison to Chla (Fig. 14a_5-e_5). On July 06, 2017, peridinin
640 was ~0.24-0.36 µg L^{-1}, accounting for high proportion of the diagnostic pigments; meanwhile, diversity of
641 marine dinoflagellate species observed from IFCB at this time was also high (Fig. 14f). However,
642 peridinin decreased (~0.001-0.05 µg L^{-1}) after the hurricane, with freshwater dinoflagellate species
643 (*Ceratium hirundinella*; Fig. 14g) detected from IFCB on September 29, 2017. In addition, maps of
644 peridinin during both surveys (Fig. 14b_5-d_5) presented higher concentration (~0.3 µg L^{-1}) in higher salinity

waters adjacent to the bay entrance, which agreed well with the increasing fraction of dinoflagellate at stations 10-14 detected from IOP inversion model (Fig. 6). In contrast, peridinin showed low concentrations in both GB and shelf waters (Fig. 14e$_5$), with dinoflagellate species rarely observed from IFCB on November 25, 2017 (Fig. 14*l*).
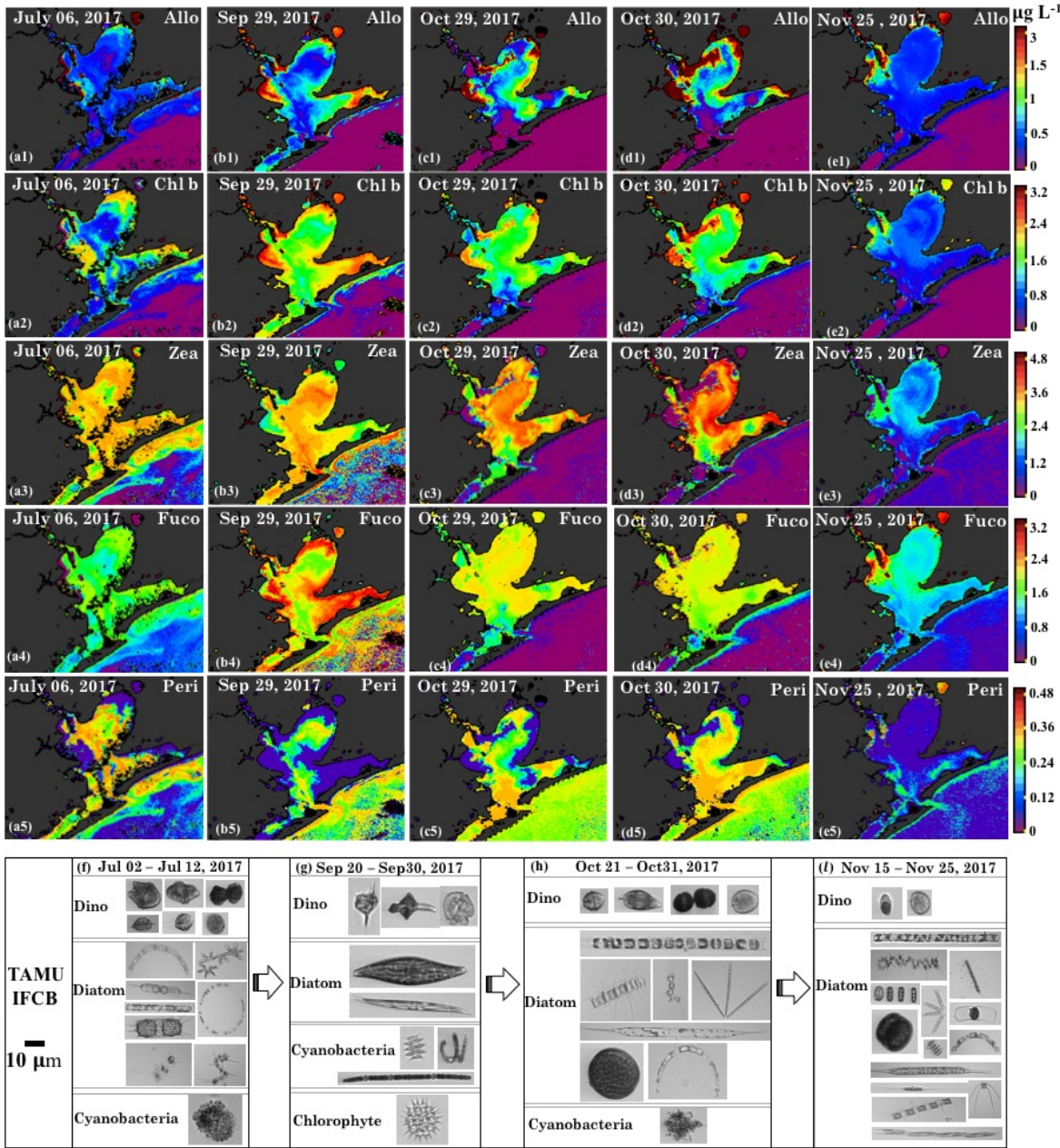
Figure 14. Sentinel-3 OLCI derived maps of diagnostic pigments for Galveston Bay. Simulated **a1-e1)** alloxanthin, **a2-e2)** Chl b, **a3-e3)** zeaxanthin, **a4-e4)** fucoxanthin, and **a5-e5)** peridinin concentrations. a, b, c, d and e represent columns (maps for July 06, September 29, October 29-30 and November 25, 2017) and 1-5 represent rows (pigments), respectively; **(f)**, **(g)**, **(h)** and **(*l*)** are the corresponding IFCB data for July 06, September 29, October 29-30 and November 25, 2017, respectively; note that IFCB pictures of fresh water species including chlorophyte and cyanobacteria that appeared on September 20-30, 2017 have been zoomed in for better clarity.

4   Discussion

4.1 Performance of the Semi-Analytical IOP Inversion Algorithm

The residuals between R_{rs_insitu} and R_{rs_mod} on September 29 and October 29-30, 2017, are negative in the blue (400-450 nm) and red (610-630 nm) spectral range at most stations, whilst keeping positive ~700 nm, which could be attributed to a number of factors. First, the underestimation near 700 nm by the IOP inversion model is possibly induced by the absence of a fluorescence component in the IOP inversion model; thus, R_{rs_insitu} containing fluorescence signals were generally higher than R_{rs_mod} near 700 nm. Second, in the range of 610-630 nm, the absorption was overestimated at most of the stations; in this spectral range, the shape of spectra was strongly modulated by cyanobacteria absorption. Thus this overestimation at ~620 nm is likely introduced by the input absorption spectrum (eigenvector) for cyanobacteria since all of input $a_{phi}^{*}(\lambda)$ are general absorption spectral shapes for different phytoplankton groups. However, the spectra of $a_{phi}^{*}(\lambda)$ can vary in magnitude and shape associated with package effects under different environmental conditions (e.g. nutrient, light and temperature) even for the same species (Bricaud et al., 2004). More detailed absorption spectra of phytoplankton under different conditions (e.g., high/low light and nutrients) could improve the performance of the IOP algorithm. Furthermore, the role of scattering might be another key factor to explain differences between R_{rs_insitu} and R_{rs_mod} for the whole spectra. The quantity and composition of suspended materials including phytoplankton, sediment and minerals will collaboratively determine $b_{bp}(\lambda)$ in both shape and magnitude. However, the input eigenvector of $b_{bp}(\lambda)$ in the present study was not divided into detailed sub-constituents and was a sum spectrum based on a power law function (Table 2). In reality, $b_{bp}(\lambda)$ spectra are not smooth and regular, and thus, the $b_{bp}(\lambda)$ value of phytoplankton and sediment might introduce errors to the whole spectrum due to their own scattering characteristics.

4.2 Distributions of NNLS-Retrieved Phytoplankton Pigments from Sentinel-3A OLCI

The NNLS-inversion algorithm showed relatively higher R^2 for those pigments that better correlated with HPLC-measured Chl a (e.g., Chl b, and alloxanthin), which was reasonably consistent with Moisan et al., 2017; this outcome could potentially be attributed to the fact that the NNLS pigment inversion algorithm was developed based on the relationship between HPLC-measured Chl a and spectrophotometer-measured $a_{pig}(\lambda)$. For instance, pigments that were relatively poorly correlated with HPLC-measured Chl a, such as fucoxanthin, diatoxanthin and diadinoxanthin on October 29-30, 2017, the OLCI-derived concentrations in cryptophyte-chlorophyte algal bloom area showed higher concentrations than those of HPLC measurements (e.g., values in gray circle; Fig. 13e), thus, resulting in lower R^2. However, in previous studies (Moisan et al., 2017; Pan et al., 2010), satellite-derived fucoxanthin appeared better correlated with HPLC-measured fucoxanthin compared to this study; it reasons that, fucoxanthin, generally one of the most abundant diatom biomarker pigments in coastal waters and along with its long-term measurements in their study area (United States northeast coast), agreed very well with Chl a. In contrast, the cryptophyte-chlorophyte algal bloom area with extremely high Chl a appeared to disturb the correlations between Chl a and fucoxanthin in this study. Also, pigments with apparent high values in algal bloom areas, such as Chl b, Chl c, alloxanthin, lutein, showed higher R^2 with RMSE less than 0.3. Thus, in-situ measurements of Chl a and $a_{pig}(\lambda)$ in waters with stronger gradients in magnitude and greater variations in phytoplankton community structures could potentially increase the challenge of applying NNLS-inversion algorithms in optically-complex estuarine waters. Further, the highly dynamic estuarine environment could as well contribute to additional uncertainties in the validation of inverted pigments due to variations such as turbulence, turbidity or light field that are likely to occur during the time interval between in-situ and Sentinel 3-OLCI (~4 hours) observations. HPLC measurements also cannot detect extremely low pigment concentrations; for example, HPLC-measured peridinin were 0.001 μgL^{-1} at several stations, however, OLCI-derived peridinin showed higher and variable values at these stations

703 (data in gray circles; Fig. 13f); this could thus increase the RMSE of the NNLS-inverted peridinin. It was
704 also found that the slope of all pigments were smaller than 1, which demonstrate that NNLS-inverted
705 pigments were relatively smaller than HPLC measurements, especially for those stations located in the
706 algal bloom area; this could most likely be attributed to the underestimation of Chl a values by the
707 Sentinel 3-OLCI empirical algorithms in the algal bloom area. Algal bloom dominated by cryptophyte
708 group, which is also known to cause red tides worldwide, to some degree, could increase red reflectance
709 and thus increase ratio values of Red/NIR and decrease estimated Chl a values. Therefore, reliable
710 estimates of satellite Chl a is crucial for the accuracy of retrieved pigments. The goal of the empirical Chl
711 a algorithm for Sentinel 3A-OLCI is to obtain more accurate estimation of surface Chl a concentration,
712 which is better for retrieving other accessory pigments. However, the primary limitation of Chl a
713 empirical algorithms in this study was that the derived relationships between Red/NIR and Chl a in GB
714 may only be valid within a specific time period due to temporally-limited field observations versus highly
715 dynamic estuarine environments. Therefore, a Chl a empirical algorithm that is more broadly applicable
716 over a longer time period will largely improve the accuracy of retrieved pigments over a series of remote
717 sensing images and can be more useful for spatiotemporal studies of phytoplankton functional diversity.
718 More importantly, the highly similar absorption spectra of many carotenoids are another key issue
719 limiting the accuracy of spectral decomposition techniques. Although the 16 input pigment spectra used
720 in this study were selected from (Thrane et al., 2015), which were correctly identified from unknown
721 phytoplankton community structure with low error rate reported from Monte Carlo tests, the potential
722 effects of aliasing spectra of some pigment pairs (e.g., fucoxanthin vs peridinin, diadinoxanthin vs lutein,
723 β-Carotene vs zeaxanthin) could still be a factor. Thus, the reported errors/R^2 for retrieved total
724 carotenoids in Trane et al., 2015 were apparently lower/higher than those of modeled total chlorophylls,
725 which showed consistency with this study. Although the predicted pigments showed a range of R^2 and
726 RMSE with known uncertainties, all are within the acceptable range and could be useful for studying the
727 spatiotemporal responses of PFTs to environmental variations, especially in such optically-complex
728 estuaries.

729 The derived maps of phytoplankton diagnostic pigments appeared to be reasonably correlated with
730 HPLC-measured diagnostic pigments and showed overall agreement with extracted phytoplankton
731 taxonomic compositions detected from the IOP inversion algorithm. The retrieved diatom-specific
732 fucoxanthin maps however, showed high concentrations compared to other pigments adjacent to the
733 entrance (Fig. 13b$_4$ and c$_4$), which contradicted with diatom %Chl a calculated from IOP inversion
734 algorithm that Chl a fraction of diatom was relatively uniform at stations 12-14 (Fig. 6b). (Nair et al.,
735 2008) concluded that fucoxanthin can occur in other phytoplankton types (e.g. raphidophyte and
736 haptophyte). Fucoxanthin and/or fucoxanthin derivatives such as 19′-hexanoyloxyfucoxanthin can also
737 replace peridinin as the major carotenoid in some dinoflagellates (e.g., Karenia brevis; Jeffrey and Vest,
738 1997). The elevated contributions from groups of dinoflagellate, haptophyte and prochlorophyte adjacent
739 to the entrance (stations 10-14; Fig. 6b) along with high concentrations of fucoxanthin likely suggest the
740 presence of elevated fractions of haptophyte and dinoflagellate, and further implies that fucoxanthin is an
741 ambiguous marker pigment for diatoms. This could also explain the poor correlation between
742 inverted %Chl a and %DP observed for the groups of diatom and haptophyte (Fig. 4g and l). These results
743 also further suggest the inherent limitations of using DP-type comparison between major biomarker
744 pigments and phytoplankton groups because the major assumption for DP-type methods is that diagnostic
745 pigment of distinct phytoplankton groups are uncorrelated to each other. This assumption is invalid in that
746 concentrations of major biomarker pigments are significantly correlated with each other and also may
747 vary in time and space under some external environmental stress (e.g., temperature, salinity, mixing, light
748 and nutrient) (Latasa and Bidigare, 1998).

749 **4.3 Response of Phytoplankton Taxa to Environmental Conditions**

750 Previous studies showed diatoms to be the most abundant taxa in GB, and tend to be more dominant
751 during winter/spring, corresponding to periods of high fresh water discharge and nutrient-replete
752 conditions (Dorado et al., 2015; Örnólfsdóttir et al., 2004a); transition from chain-forming diatoms such
753 as *Chaetoceros* and rod-like diatoms pre-flood to small cells, such as *Thalassiosira* and small pennate
754 diatoms were generally observed during high river discharge periods (Anglès et al., 2015; Lee, 2017). In
755 contrast, cyanobacteria were the most abundant species during the warmer months (Jun-Aug) when river
756 discharge was relatively low (Örnólfsdóttir et al., 2004b). Further, phytoplankton groups in GB responded
757 differentially both taxonomically and spatially to the freshening events due to their contrasting nutrient
758 requirements and specific growth characteristics. For instance, most phytoplankton taxa (e.g., diatom,
759 chlorophyte and cryptophyte) can be positively stimulated by fresh inflows due to their relatively rapid
760 growth rate (Paerl et al., 2003); however, Roelke et al. (2013) also documented that cyanobacteria and
761 haptophytes in the upper GB were not sensitive to nutrient-rich waters from both rivers, due to the extra
762 nutrients obtained from N_2-fixation abilities and mixotrophic characteristics, respectively. In the lower
763 part of GB, dinoflagellates and cyanobacteria are known to be more dominant during the low river
764 discharge due to their preference for higher phosphorus (P) compared to some other groups, and to low
765 turbulence (Lee, 2017) and thus, generally inversely related to the fresh inflows (Lee, 2017; Roelke et al.,
766 2013).

767 Perturbations following Hurricane Harvey affected the phytoplankton taxonomic composition with
768 alterations in phytoplankton community structure observed as the GB system transitioned from marine to
769 freshwater then to marine system (Figs. 6 and 14). Higher fraction of zeaxanthin and peridinin and the
770 presence of large and slow-growing marine dinoflagellates detected from IFCB pre-hurricane (July 06,
771 2017) indicate that both cyanobacteria and dinoflagellates were the main groups of phytoplankton
772 community during summer, and likely associated with warmer temperature and lower river flow (Lee,
773 2017). Later, massive Chla observed in September, 2017 and the decline of Chla to background state in
774 October, 2017, were likely associated with the hurricane-induced high river discharge and the resulting
775 variations in nutrient concentration and composition. Higher fractions of diatom and chlorophyte
776 accompanied with increasing fucoxanthin and Chl b on September 29, 2017, to some extent agreed well
777 with measurements of Steichen et al., 2018 two weeks following Hurricane Harvey that freshwater
778 species (diatom, green algae and cyanobacteria) appeared immediately following the flooding event.
779 Greater abundance of diatom and chlorophyte during survey 1 in comparison to survey 2 were likely due
780 to their rapid growth rates, enhanced nutrient uptake rates, and tolerance of low salinity and high
781 turbulence under high nutrient loading conditions following the freshwater inflows (Roy et al., 2013;
782 Santschi, 1995). Therefore, it is not surprising that Chl b concentrations showed very low values in July
783 and November, 2017, when river discharge was correspondingly low. Cyanobacteria, which normally
784 prefer low salinity conditions, also showed specific responses to this flood event. On September 29, 2017,
785 zeaxanthin slightly increased compared to summer season in July, 2017. The decline of diatoms and
786 chlorophyte versus slightly increased cyanobacteria observed on October 29-30, 2017, could be attributed
787 to the relatively slow growth rates of cyanobacteria compared to that of chlorophytes and diatom (Paerl et
788 al., 2003); cyanobacteria appeared to have lagged behind these groups in terms of responding to enhanced
789 freshwater discharge when longer residence times were again restored. In contrast, the presence of green
790 algae and cyanobacteria could as well as be explained by the clarity and turbidity gradient of water. Quigg
791 et al. (2010) reported that when turbidity was relatively high, chlorophyte dominated over cyanobacteria
792 with biomass ratio of chlorophyte/cyanobacteria greater than 2, which supported our observations that
793 chlorophyte dropped off whilst cyanobacteria increased during survey 2 on October 29-30, 2017. In
794 addition, highest cyanobacteria percentage in East Bay suggest that calm and stratified waters may
795 accelerate cyanobacteria growth as the buoyancy regulation mechanism of cyanobacteria is possibly
796 restricted by the water mixing (Roy et al., 2013). Peridinin, which initially decreased in September and
797 then increased in the lower GB on October 29-30, 2017, suggest that dinoflagellates showed overall
798 preference for high-salinity waters. Furthermore, previous IFCB observations from Biological and
799 Chemical Oceanography Data Management Office (BCO-DMO) showed that algal blooms after

800 hurricanes in the nGOM were initially dominated by diatoms, and subsequently transitioned to blooms of
801 dinoflagellates, likely associated with nutrient ratios and chemical forms of nutrient supplied by the flood
802 waters and rainfall (Heisler et al., 2008). In addition, high concentrations of peridinin observed along the
803 Houston Ship Channel, might provide evidence that the ballast water addition from shipping vessels
804 likely promote harmful species of dinoflagellates (Steichen et al., 2015). Finally, low concentrations of all
805 pigments on November 25, 2017 with relatively higher fraction of fucoxanthin compared to previous
806 dates (Fig. 14), indicate the major role of marine diatoms at that time and further confirms that diatoms
807 can be found under a wide range of inflows in GB.

808 The localized cryptophyte-chlorophyte bloom that occurred ~60d after Hurricane Harvey on October 29-
809 30, 2017, was captured by both satellite and in-situ measurements. This bloom might not be associated
810 with the flooding events of Hurricane Harvey, and could be linked to nutrient-rich runoff flowing into GB,
811 reflecting sensitivity and rapid response of phytoplankton community to nutrient input in GB. In shallow
812 and turbid estuaries, human activities are altering the environment and causing phytoplankton changes in
813 diversity and biomass to occur more frequently. Dugdale et al. (2012) reported that variations of
814 phytoplankton community in San Francisco estuary could be attributed to anthropogenically-elevated
815 concentration of ammonium, which restrain the uptake of nitrate, thus reducing the growth and
816 reproduction of larger diatoms and shifting towards smaller species (e.g., cryptophyte and green
817 flagellate). Furthermore, 'pink oyster' events related to alloxanthin of cryptophyte in GB occurred more
818 frequently from September through October in recent years (Paerl et al., 2003). The eastern side of
819 Houston Channel in mid bay region was reported as the area most heavily impacted by the intense 'pink
820 oyster' events. Previous studies and present observations both suggest that this cryptophyte-chlorophyte
821 dominated bloom could be promoted by the nutrient-driven eutrophication from Houston Ship Channel,
822 urbanization and industrialization along the upper San Jacinto River complex.

823 **4.4 Photo-Physiological State of Natural Phytoplankton Community**

824 In this study, the CDOM-corrected F_V/F_M and σ_{PSII} likely represented a composite of both phytoplankton
825 taxonomy and physiological stress (e.g., nutrient and mixing). Typically, lowest N and P concentrations
826 were measured closest to the nGOM (Quigg et al., 2009). Phytoplankton community living close to
827 nGOM were usually in poor nutrient conditions and would be expected to maximize their light harvesting
828 (increase in σ_{PSII}) due to nutrient stress. Simultaneously, phytoplankton cells might experience a decline
829 of functional proportion of reaction centers of PSII (RCII), which means decrease in F_V/F_M. The observed
830 low levels of F_V/F_M and Chl a/TP versus high values of σ_{PSII} and AP/TP adjacent to the nGOM showed
831 agreement with previous studies that the fraction of carotenoids to be higher for nutrient-poor cultures
832 (Schitüter et al., 1997; Holmboe et al., 1999). In contrast, phytoplankton in well-mixed waters (station 7-9)
833 might experience abundant nutrients due to the resuspension of cyclonic gyre around Smith Points; as
834 such, their photosynthetic machinery were likely healthier. Aiken et al. (2004) documented that the Chl
835 a/TP ratio was relatively higher when plants were in good growing conditions, which is similar to the
836 observations in this study that phytoplankton have higher fraction of Chl a accompanying higher rate of
837 photosynthetic efficiency (F_V/F_M) under nutrient replete conditions. Overall, the spatial pattern of F_V/F_M
838 and σ_{PSII} in GB could be mainly attributed to physiological stress of nutrient and hydrodynamics
839 conditions since the light availability (PAR) during the sampling period did not spatially vary
840 significantly at the surface. Furthermore, FIRe measurements (F_V/F_M and σ_{PSII}) also presented a
841 taxonomic signal super-imposed upon environmental factors. Each cluster with different dominant taxa
842 (well mixed group, chlorophyte & cryptophyte, cyanobacteria, and dinoflagellate & haptophyte)
843 displayed different physiological characteristics. The taxonomic sequence of eukaryotic groups from high
844 F_V/F_M, low σ_{PSII} to low F_V/F_M, high σ_{PSII} in the present observations showed potential effects of
845 phytoplankton cell size corresponding to diatoms, chlorophyte, and cryptophyte, dinoflagellate and
846 haptophyte. The prokaryote (cyanobacteria) had relatively high values of F_v/F_m and low values of σ_{PSII};

847 this agreed with F_V/F_M for some species of nitrogen-fixing cyanobacteria that can range from 0.6 to 0.65
848 (Berman-Frank et al., 2007). Yet, it is difficult to separate the contributions from environmental factors
849 and taxonomic variations to the changes of FIRe fluorescence signals since all these parameters are inter-
850 related. Different phytoplankton groups/sizes will display distinct physiological traits (F_V/F_M and σ_{PSII})
851 when experiencing considerable environmental pressures. Thus, effects of physiological stress on
852 F_V/F_M and σ_{PSII} variations for natural samples can only be determined when taxonomic composition can
853 be excluded as a contributor (Suggett et al., 2009).

5   Conclusions

855 Field measurements (salinity, pigments, optical properties and physiological parameters) and ocean color
856 observations from Sentinel-3A OLCI were used to study the effects of extreme flooding associated with
857 Hurricane Harvey on the phytoplankton community structures, pigment distributions and their
858 physiological state in GB. Flooding effects made the entire GB transition from saline to freshwater then
859 back to a more marine influenced system. The band ratio (Red/NIR) of R_{rs_insitu} were negatively correlated
860 with HPLC-measured Chl a in an exponential relationship ($R^2 > 0.93$). The satellite-retrieved Chl a maps
861 yielded much higher Chl a concentration on September 29, 2017 compared to October 29-30, 2017 with
862 lowest Chl a observed adjacent to the shelf waters. Phytoplankton taxonomic composition was further
863 retrieved from R_{rs_insitu} using a 10-species IOP inversion algorithm. Phytoplankton community generally
864 dominated by estuarine marine diatoms/dinoflagellates before flood events, was altered to freshwater
865 species of diatom, green algae (chlorophyte) and cyanobacteria during survey 1. It also showed an
866 increase of small-size species including cryptophyte, haptophyte, prochlorophyte and cyanobacteria
867 accompanied by a decline of chlorophyte and diatoms during survey 2.

868 Phytoplankton diagnostic pigments were retrieved using an NNLS inversion model based on Sentinel-3A
869 OLCI Chl a maps also confirmed spatiotemporal variations of phytoplankton taxonomy. The NNLS-
870 retrieved diagnostic pigment maps showed overall spatiotemporal agreement with HPLC measurements
871 with R^2 ranging from 0.40 (diatoxanthin) to 0.96 (Chl a) during both surveys. Alloxanthin, Chl b, and
872 fucoxanthin exhibiting similar patterns with Chla, showed different levels of increase after Hurricane
873 Harvey. In contrast, NNLS-derived zeaxanthin and peridinin presented significantly low values in the
874 area where Chla concentrations were high. Further, maps of zeaxanthin and peridinin displayed relatively
875 higher fraction on July 06, 2017 before the hurricane compared to other diagnostic pigments. However,
876 peridinin decreased post-hurricane on September 29, 2017 and then increased a bit on October 29-30,
877 2017. Ultimately, concentration of Chl a and all biomarker pigments decreased to low levels in November,
878 2017 when the typical environmental conditions of GB was restored.

879 Finally, the retrieved phytoplankton taxonomic compositions from IOP inversion algorithm were linked
880 with FIRe-measured photosynthetic parameters (F_V/F_M and σ_{PSII}) to assess the effects of physiological
881 stress and taxonomic contributions on phytoplankton photosynthetic performance. An inverse relationship
882 between the F_V/F_M and σ_{PSII} were observed during both surveys. Phytoplankton community in well-
883 mixed waters (around Smith Point) showed high F_V/F_M against low σ_{PSII}; in contrast, the area with poor
884 nutrient conditions (adjacent to the shelf waters), showed low F_V/F_M and elevated σ_{PSII}. Taxonomic
885 signatures of F_v/F_m and σ_{PSII} revealed diverse physiological characteristics with dinoflagellate-
886 haptophyte group showing the lowest F_V/F_M versus the highest σ_{PSII}, whereas prokaryote of
887 cyanobacteria-dominated group showed high values of F_V/F_M and low values of σ_{PSII}. Overall, this study
888 using field and ocean color data combined with inversion algorithms provided novel insights on
889 phytoplankton response to an extreme flood perturbation in a turbid estuarine environment based on
890 taxonomy, pigment composition and physiological state of phytoplankton.

891

892 *Data availability.* Data from field measurements are available upon request from the corresponding
893 author.

894
895 *Author contributions.* BL and ED conceived and designed the research; BL, ED and IJ collected and
896 processed the data; BL analyzed the data and all authors contributed to writing the paper.

897
898 *Competing interests.* The authors declare that they have no conflict of interest.

899 *Acknowledgements.* The authors thank the European Space Agency (ESA) and the European Organization
900 for Meteorological Satellites (EUMESAT) for providing access to the Sentinel-3 OLCI ocean color data
901 and the Sentinel-3 Toolbox Kit Module (S3TBX) version 5.0.1 in Sentinel Application Platform (SNAP).
902 We also would like to thank Phytoplankton Dynamics Lab of Texas A&M University, Galveston Campus,
903 for the near-real time microplankton pictures recorded by an Imaging FlowCytobot, which are made
904 available on the web. We are grateful to Bill Gibson from the Coastal Studies Institute for providing
905 logistic support for field operations. EJD acknowledges NASA support through grant No.
906 80NSSC18K0177.

907

908 **References**

909 Acker, J., Lyon, P., Hoge, F., Shen, S., Roffer, M., and Gawlikowski, G.: Interaction of Hurricane Katrina with
910 optically complex water in the Gulf of Mexico: interpretation using satellite-derived inherent optical properties
911 and chlorophyll concentration, IEEE Geosci. and Remote Sens. Lett., 6, 209-213, 2009.
912 Aiken, J., Fishwick, J., Moore, G., and Pemberton, K.: The annual cycle of phytoplankton photosynthetic
913 quantum efficiency, pigment composition and optical properties in the western English Channel, J. Mar. Biol.
914 Assoc. U. K., 84, 301-313, 2004.
915 Alvain, S., Moulin, C., Dandonneau, Y., and Bréon, F.-M.: Remote sensing of phytoplankton groups in case 1
916 waters from global SeaWiFS imagery, Deep Sea Res., Part I, 52, 1989-2004, 2005.
917 Anglès, S., Jordi, A., and Campbell, L.: Responses of the coastal phytoplankton community to tropical
918 cyclones revealed by high-frequency imaging flow cytometry, Limnology and Oceanography, 60, 1562-1576,
919 2015.
920 Barlow, R., Cummings, D., and Gibb, S.: Improved resolution of mono-and divinyl chlorophylls a and b and
921 zeaxanthin and lutein in phytoplankton extracts using reverse phase C-8 HPLC, Mar. Ecol. Progr. Ser., 161,
922 303-307, 1997.
923 Behrenfeld, M. J., and Falkowski, P. G.: Photosynthetic rates derived from satellite-based chlorophyll
924 concentration, Limnol. Oceanogr., 42, 1-20, 1997.
925 Behrenfeld, M. J., and Kolber, Z. S.: Widespread iron limitation of phytoplankton in the South Pacific Ocean,
926 Science, 283, 840-843, 1999.
927 Berman-Frank, I., Quigg, A., Finkel, Z. V., Irwin, A. J., and Haramaty, L.: Nitrogen-fixation strategies and Fe
928 requirements in cyanobacteria, Limnol. Oceanogr., 52, 2260-2269, 2007.
929 Bidigare, R. R., Ondrusek, M. E., Morrow, J. H., and Kiefer, D. A.: In-vivo absorption properties of algal
930 pigments, Ocean Optics X, Intl. Soc. Opt. Photonics., 1302, 290-303, 1990.
931 Blondeau-Patissier, D., Gower, J. F., Dekker, A. G., Phinn, S. R., and Brando, V. E.: A review of ocean color
932 remote sensing methods and statistical techniques for the detection, mapping and analysis of phytoplankton blooms
933 in coastal and open oceans, Progr. Oceanogr., 123, 123-144, 2014.
934 Bracher, A., Taylor, M., Taylor, B., Dinter, T., Roettgers, R., and Steinmetz, F.: Using empirical orthogonal
935 functions derived from remote sensing reflectance for the prediction of phytoplankton pigments concentrations,
936 Ocean Sci., 11, 139-158, 2015.
937 Brewin, R. J., Sathyendranath, S., Hirata, T., Lavender, S. J., Barciela, R. M., and Hardman-Mountford, N. J.: A
938 three-component model of phytoplankton size class for the Atlantic Ocean, Ecol. Modell., 221, 1472-1483, 2010.

939 Bricaud, A., Claustre, H., Ras, J., and Oubelkheir, K.: Natural variability of phytoplanktonic absorption in oceanic
940 waters: Influence of the size structure of algal populations, J. Geophys. Res. Oceans, 109, C11010–1, 2004.
941 Campbell, D., Hurry, V., Clarke, A. K., Gustafsson, P., and. Öquist, G.: Chlorophyll fluorescence analysis of
942 cyanobacterial photosynthesis and acclimation, Microbiol. Molecul. Biol. Rev., 62, 667-683, 1988.
943 Carder, K. L., Chen, F., Lee, Z., Hawes, S., and Kamykowski, D.: Semianalytic Moderate-Resolution Imaging
944 Spectrometer algorithms for chlorophyll a and absorption with bio-optical domains based on nitrate-depletion
945 temperatures, J. Geophys. Res. Oceans, 104, 5403-5421, 1999.
946 Chase, A., Boss, E., Zaneveld, R., Bricaud, A., Claustre, H., Ras, J., Dall'Olmo, G., and Westberry, T. K.:
947 Decomposition of in situ particulate absorption spectra, Meth. Oceanogr., 7, 110-124, 2013.
948 Chase, A., Boss, E., Cetinić, I., and Slade, W.: Estimation of phytoplankton accessory pigments from hyperspectral
949 reflectance spectra: toward a global algorithm, J. Geophys. Res. Oceans, 122, 9725-9743, 2017.
950 Ciotti, A. M., Lewis, M. R., and Cullen, J. J.: Assessment of the relationships between dominant cell size in natural
951 phytoplankton communities and the spectral shape of the absorption coefficient, Limnol. Oceanogr., 47, 404-417,
952 2002.
953 Cullen, J. J., and Davis, R. F.: The blank can make a big difference in oceanographic measurements, Limnol.
954 Oceanogr., 12, 29-35, 2003.
955 D'Sa, E. J., Lohrenz, S. E., Asper, V. L., and Walters, R. A.: Time series measurements of chlorophyll fluorescence
956 in the oceanic bottom boundary layer with a multisensor fiber-optic fluorometer, J. Atmos. Ocean. Technol., 14,
957 889-896, 1997.
958 D'Sa, E. J., and Lohrenz, S. E.: Theoretical treatment of fluorescence detection by a dual-fiber-optic sensor with
959 consideration of sampling variability and package effects associated with particles, Appl. Optics, 38, 2524-2535,
960 1999.
961 D'Sa, E. J., Miller, R. L., and Del Castillo, C.: Bio-optical properties and ocean color algorithms for coastal waters
962 influenced by the Mississippi River during a cold front, Appl. Optics, 45, 7410-7428, 2006.
963 D'Sa, E. J., Korobkin, M., and Ko, D. S.: Effects of Hurricane Ike on the Louisiana–Texas coast from satellite and
964 model data, Remote Sens. Lett., 2, 11-19, 2011.
965 D'Sa, E. J.: Assessment of chlorophyll variability along the Louisiana coast using multi-satellite data, GISci. Remote
966 Sens., 51, 139-157, 2014.
967 D'Sa, E. J., Joshi, I., and Liu, B.: Galveston Bay and coastal ocean optical- geochemical response to Hurricane
968 Harvey from VIIRS ocean color, Geophys. Res. Lett., 45, 10579-10589, https://doi.org/10.1029/2018GL079954,
969 2018.
970 Devred, E., Sathyendranath, S., Stuart, V., and Platt, T.: A three component classification of phytoplankton
971 absorption spectra: Application to ocean-color data, Remote Sens. Environ., 115, 2255-2266, 2011.
972 Dierssen, H. M., Kudela, R. M., Ryan, J. P., and Zimmerman, R. C.: Red and black tides: Quantitative analysis of
973 water-leaving radiance and perceived color for phytoplankton, colored dissolved organic matter, and suspended
974 sediments, Limnol. Oceanogr., 51, 2646-2659, 2006.
975 Doerffer, R., and Schiller, H.: The MERIS Case 2 water algorithm, Intl. J. Remote Sens., 28, 517-535, 2007.
976 Dorado, S., Booe, T., Steichen, J., McInnes, A. S., Windham, R., Shepard, A., Lucchese, A. E., Preischel, H.,
977 Pinckney, J. L., and Davis, S. E.: Towards an understanding of the interactions between freshwater inflows and
978 phytoplankton communities in a subtropical estuary in the Gulf of Mexico, PLoS One, 10, e0130931, 2015.
979 Dugdale, R., Wilkerson, F., Parker, A. E., Marchi, A., and Taberski, K.: River flow and ammonium discharge
980 determine spring phytoplankton blooms in an urbanized estuary, Estuar. Coast. Shelf Sci., 115, 187-199, 2012.
981 Dutkiewicz, S., Hickman, A. E., Jahn, O., Gregg, W. W., Mouw, C. B., and Follows, M. J.: Capturing optically
982 important constituents and properties in a marine biogeochemical and ecosystem model, Biogeosciences, 12, 4447-
983 4481, 2015.
984 Farfan, L. M., D'Sa, E. J., and Liu, K.: Tropical cyclone impacts on coastal regions: the case of the Yucatan and the
985 Baja California Peninsulas. Mexico, Estuar. Coast., 37, 1388-1402, 2014.
986 Ficek, D., Kaczmarek, S. a., Stoñ-Egiert, J., Wozniak, B., Majchrowski, R., and Dera, J.: Spectra of light absorption
987 by phytoplankton pigments in the Baltic; conclusions to be drawn from a Gaussian analysis of empirical data,
988 Oceanologia, 46, 533-555, 2004.
989 Fishwick, J. R., Aiken, J., Barlow, R., Sessions, H., Bernard, S., and Ras, J.: Functional relationships and bio-optical
990 properties derived from phytoplankton pigments, optical and photosynthetic parameters; a case study of the
991 Benguela ecosystem, J. Mar. Biol. Assoc. U. K., 86, 1267-1280, 2006.
992 Garver, S. A., and Siegel, D. A.: Inherent optical property inversion of ocean color spectra and its biogeochemical
993 interpretation: 1. Time series from the Sargasso Sea, J. Geophys. Res., Oceans, 102, 18607-18625, 1997.

994   Geider, R. J., La Roche, J., Greene, R. M., and Olaizola, M.: Response of the photosynthetic apparatus of
995   phaeodactylum tricornutum (bacillariophyceae to nitrate, phosphate, or iron starvation, J. Phycol., 29, 755-766, 1993.
996   Gilerson, A. A., Gitelson, A. A., Zhou, J., Gurlin, D., Moses, W., Ioannou, I., and Ahmed, S. A.: Algorithms for
997   remote estimation of chlorophyll-a in coastal and inland waters using red and near infrared bands, Opt. Express, 18,
998   24109-24125, 2010.
999   Gitelson, A.: The peak near 700 nm on radiance spectra of algae and water: relationships of its magnitude and
1000   position with chlorophyll concentration, Int. J. Remote Sens., 13, 3367-3373, 1992.
1001   Gordon, H. R., Brown, O. B., Evans, R. H., Brown, J. W., Smith, R. C., Baker, K. S., and Clark, D. K.: A
1002   semianalytic radiance model of ocean color, J. Geophys. Res., Atmos., 93, 10909-10924, 1988.
1003   Guthrie, C. G., Matsumoto, J., and Solis, R.: Analysis of the influence of water plan strategies on inflows and
1004   salinity in Galveston Bay, Final report to the United States Army Corps of Engineers, Contract #R0100010015.
1005   Texas Water Development Board, Austin, Texas, USA, 71 pp., 2012.
1006   Heisler, J., Glibert, P. M., Burkholder, J. M., Anderson, D. M., Cochlan, W., Dennison, W. C., and Lewitus, A.:
1007   Eutrophication and harmful algal blooms: a scientific consensus, Harmful Algae, 8, 3-13, 2008.
1008   Hirata, T., Aiken, J., Hardman-Mountford, N., Smyth, T. J., and. Barlow, R. G.: An absorption model to determine
1009   phytoplankton size classes from satellite ocean colour, Remote Sens. Environ., 112, 3153–3159, 2008.
1010   Hirata, T., Hardman-Mountford, N., Brewin, R., Aiken, J., Barlow, R., Suzuki, K., Isada, T., Howell, E., Hashioka,
1011   T., Noguchi-Aita, M., and Yamanaka, Y.: Synoptic relationships between surface Chlorophyll-a and diagnostic
1012   pigments specific to phytoplankton functional types. Biogeosciences, 8, 311–327, 2011.
1013   Hoepffner, N., and Sathyendranath, S.: Effect of pigment composition on absorption properties of phytoplankton,
1014   Mar. Ecol. Progr. Ser., 73, l-23, 1991.
1015   Hoge, F. E., and Lyon, P. E.: Satellite retrieval of inherent optical properties by linear matrix inversion of oceanic
1016   radiance models: an analysis of model and radiance measurement errors, J. Geophys. Res., Oceans, 101, 16631-
1017   16648, 1996.
1018   Holmboe, N., Jensen, H. S., and Andersen, F. Ø.: Nutrient addition bioassays as indicators of nutrient limitation of
1019   phytoplankton in a eutrophic estuary, Mar. Ecol. Progr. Ser., 186, 95-104, 1999.
1020   Howarth, R. W., Marino, R., Lane, J., and Cole, J. J.: Nitrogen fixation in freshwater, estuarine, and marine
1021   ecosystems. 1. Rates and importance, Limnol. Oceanogr., 33, 669-687, 1988.
1022   Hu, C., Cannizzaro, J., Carder, K. L., Muller-Karger, F. E., and Hardy, R.: Remote detection of Trichodesmium
1023   blooms in optically complex coastal waters: Examples with MODIS full-spectral data, Remote Sens. Environ., 114,
1024   2048-2058, 2010.
1025   Hu, C., and Feng, L.: Modified MODIS fluorescence line height data product to improve image interpretation for
1026   red tide monitoring in the eastern Gulf of Mexico, J. Appl. Remote Sens., 11, 012003, 2016.
1027   Jeffrey, S., and Vest, M.: Introduction to marine phytoplankton and their pigment signatures, in: Phytoplankton
1028   pigment in oceanography, edited by: Jeffrey, S.W., Mantoura, R. F. C., and Wright, S. W., UNESCO Publishing,
1029   Paris, France, 37-84, 1997.
1030   Joshi, I. D., and D'Sa, E. J.: Seasonal variation of colored dissolved organic matter in Barataria Bay, Louisiana,
1031   using combined Landsat and field data, Remote Sens., 7, 12478-12502, 2015.
1032   Joshi, I. D., D'Sa, E. J., Osburn, C. L., Bianchi, T. S., Ko, D. S., Oviedo-Vargas, D., Arellano, A. R., and Ward, N.
1033   D.: Assessing chromophoric dissolved organic matter (CDOM) distribution, stocks, and fluxes in Apalachicola Bay
1034   using combined field, VIIRS ocean color, and model observations, Remote Sens. Environ., 191, 359-372, 2017.
1035   Joshi, I. D., and D'Sa, E. J.: An estuarine tuned Quasi-Analytical Algorithm for VIIRS (QAA-V): assessment and
1036   application to satellite estimates of SPM in Galveston Bay following Hurricane Harvey. Biogeosciences, 15, 4065-
1037   4086, 2018.
1038   Kolber, Z. S., Zehr, J., and Falkowski, P. G.: Effects of growth irradiance and nitrogen limitation on photosynthetic
1039   energy conversion in photosystem II, Plant Physiol., 88, 923-929, 1988.
1040   Kolber, Z. S., Prášil, O., and Falkowski, P. G.: Measurements of variable chlorophyll fluorescence using fast
1041   repetition rate techniques: defining methodology and experimental protocols, Biochim. Biophys. Acta (BBA)-
1042   Bioenergetics, 1367, 88-106, 1998.
1043   Latasa, M., and Bidigare, R. R.: A comparison of phytoplankton populations of the Arabian Sea during the Spring
1044   Intermonsoon and Southwest Monsoon of 1995 as described by HPLC-analyzed pigments, Deep Sea Res., Part II,
1045   45, 2133-2170, 1998.
1046   Lee, Z., Carder, K. L., Peacock, T., Davis, C., and Mueller, J.: Method to derive ocean absorption coefficients from
1047   remote-sensing reflectance, Appl. Optics, 35, 453-462, 1996.
1048   Lee, Z., Carder, K. L., and Arnone, R. A.: Deriving inherent optical properties from water color: a multiband quasi-
1049   analytical algorithm for optically deep waters, Appl. Optics, 41, 5755-5772, 2002.

1050 Lee, H. A.: Effects of Physical Disturbance on Phytoplankton Diversity and Community Composition in Galveston
1051 Bay, TX, during an Extreme Flooding Event, Diss., 2017.
1052 Lohrenz, S. E., Weidemann, A. D., and Tuel, M.: Phytoplankton spectral absorption as influenced by community
1053 size structure and pigment composition J. Plankton Res., 25, 35-61, 2003.
1054 Lutz, V. A., Sathyendaranath, S., Head, E. J., and Li, W. K.: Changes in the in vivo absorption and fluorescence
1055 excitation spectra with growth irradiance in three species of phytoplankton, J. Plankton Res., 23, 555-569, 2001.
1056 Mackey, M., Mackey, D., Higgins, H., and Wright, S.: CHEMTAX-a program for estimating class abundances from
1057 chemical markers: application to HPLC measurements of phytoplankton, Mar. Ecol. Progr. Ser., 144, 265-283, 1996.
1058 Maritorena, S., Siegel, D. A., and Peterson, A. R.: Optimization of a semianalytical ocean color model for global-
1059 scale applications, Appl. Optics, 41, 2705-2714, 2002.
1060 Moisan, T. A., Moisan, J. R., Linkswiler, M. A., and Steinhardt, R. A.: Algorithm development for predicting
1061 biodiversity based on phytoplankton absorption, Cont. Shelf Res., 55, 17-28, 2013.
1062 Moisan, T. A., Rufty, K. M., Moisan, J. R., and Linkswiler, M. A.: Satellite observations of phytoplankton
1063 functional type spatial distributions, phenology, diversity, and ecotones, Front. Mar. Sci., 4, 189, 2017.
1064 Moore, C. M., Suggett, D. J., Holligan, P. M., Sharples, J., Abraham, E. R., Lucas, M. I., Rippeth, T. P., Fisher, N.
1065 R., Simpson, J. H., and Hydes, D. J.: Physical controls on phytoplankton physiology and production at a shelf sea
1066 front: a fast repetition-rate fluorometer based field study, Mar. Ecol. Progr. Ser., 259, 29-45, 2003.
1067 Moore, C. M., Suggett, D. J., Hickman, A. E., Kim, Y.-N., Tweddle, J. F., Sharples, J., Geider, R. J., and Holligan, P.
1068 M.: Phytoplankton photoacclimation and photoadaptation in response to environmental gradients in a shelf sea,
1069 Limnology and Oceanography, 51, 936-949, 2006.
1070 Morel, A., and Prieur, L.: Analysis of variations in ocean color 1, Limnol. Oceanogr., 22, 709-722, 1977.
1071 Nair, A., Sathyendranath, S., Platt, T., Morales, J., Stuart, V., Forget, M.-H., Devred, E., and Bouman, H.: Remote
1072 sensing of phytoplankton functional types, Remote Sens. Environ., 112, 3366-3375, 2008.
1073 Örnólfsdóttir, E. B., Pinckney, J. L., and Tester, P. A.: Quantification of the relative abundance of the toxic
1074 dinoflagellate, karenia brevis (dinophyta), using unique photopigments, J. Phycol., 39, 449-457, 2003.
1075 Örnólfsdóttir, E. B., Lumsden, S. E., and Pinckney, J. L.: Nutrient pulsing as a regulator of phytoplankton
1076 abundance and community composition in Galveston Bay, Texas, J. Experiment. Mar. Biol. Ecol., 303, 197-220,
1077 2004a.
1078 Örnólfsdóttir, E. B., Lumsden, S. E., and Pinckney, J. L.: Phytoplankton community growth-rate response to nutrient
1079 pulses in a shallow turbid estuary, Galveston Bay, Texas, J. Plankton Res., 26, 325-339, 2004b.
1080 Paerl, H. W., Valdes, L. M., Pinckney, J. L., Piehler, M. F., Dyble, J., and Moisander, P. H.: Phytoplankton
1081 photopigments as indicators of estuarine and coastal eutrophication, AIBS Bull., 53, 953-964, 2003.
1082 Pan, X., Mannino, A., Russ, M. E., Hooker, S. B., and Harding Jr, L. W.: Remote sensing of phytoplankton pigment
1083 distribution in the United States northeast coast, Remote Sens. Environ., 114, 2403-2416, 2010.
1084 Pan, X., Mannino, A., Marshall, H. G., Filippino, K. C., and Mulholland, M. R.: Remote sensing of phytoplankton
1085 community composition along the northeast coast of the United States, Remote Sens. Environ., 115, 3731-3747,
1086 2011.
1087 Quigg, A., Roelke, D., and Davis, S. E.: Freshwater inflows and the health of Galveston Bay: influence of nutrient
1088 and sediment load on the base of the food web, Final report of the coastal coordination council pursuant to National
1089 Oceanic and Atmospheric Administration Award No. NA07NOS4190144, Texas A&M University at Galveston,
1090 Texas, USA, 49 pp., 2009.
1091 Quigg, A., Litherland, S., Phillips, J., and Kevekordes, K.: Phytoplankton productivity across Moreton Bay,
1092 Queensland, Australia: the impact of water quality, light and nutrients on spatial patterns, in: Proceedings of the 13th
1093 International Marine Biological Workshop, Moreton Bay, Queensland, Australia, 7-25 February, 2005, 355-372,
1094 2010.
1095 Quigg, A. S.: Understanding the role of nutrients in defining phytoplankton responses in the Trinity-San Jacinto
1096 Estuary, Final report to Interagency Cooperative Contract No. 1104831134, Texas A & M University at Galveston,
1097 Texas, USA, 56 pp., 2011.
1098 Rayson, M. D., Gross, E. S., Hetland, R. D., and Fringer, O. B.: Time scales in Galveston Bay: An unsteady estuary,
1099 J. Geophys. Res., Oceans, 121, 2268–2285, 2016.
1100 Ritchie, R. J.: Consistent sets of spectrophotometric chlorophyll equations for acetone, methanol and ethanol
1101 solvents, Photosynthesis Res., 89, 27-41, 2006.
1102 Roelke, D. L., Li, H.-P., Hayden, N. J., Miller, C. J., Davis, S. E., Quigg, A., and Buyukates, Y.: Co-occurring and
1103 opposing freshwater inflow effects on phytoplankton biomass, productivity and community composition of
1104 Galveston Bay, USA, Mar. Ecol. Progr. Ser., 477, 61-76, 2013.

1105 Roesler, C. S., and Perry, M. J.: In situ phytoplankton absorption, fluorescence emission, and particulate
1106 backscattering spectra determined from reflectance, J. Geophys. Res., Oceans, 100, 13279-13294, 1995.
1107 Roesler, C. S., and Boss, E.: Spectral beam attenuation coefficient retrieved from ocean color inversion, Geophys.
1108 Res. Lett., 30, 2003.
1109 Roesler, C. S., Etheridge, S. M., and Pitcher, G. C.: Application of an ocean color algal taxa detection model to red
1110 tides in the Southern Benguela, in: Proceedings of the Xth International Conference on Harmful Algae, Florida Fish
1111 and Wildlife Conservation Commission and Intergovernmental Oceanographic Commission of UNESCO, St.
1112 Petersburg, Florida, USA, October, 2002, 303-305, 2003.
1113 Roy, E. D., White, J. R., Smith, E. A., Bargu, S., and Li, C.: Estuarine ecosystem response to three large-scale
1114 Mississippi River flood diversion events, Sci. Total Environ., 458, 374-387, 2013.
1115 Santschi, P. H.: Seasonality in nutrient concentrations in Galveston Bay, Mar. Environ. Res., 40, 337-362, 1995.
1116 Sathyendranath, S., Aiken, J., Alvain, S., Barlow, R., Bouman, H., Bracher, A., Brewin, R., Bricaud, A., Brown, C.,
1117 and Ciotti, A.: Phytoplankton functional types from Space, in: (Reports of the International Ocean-Colour
1118 Coordinating Group (IOCCG); 15), International Ocean-Colour Coordinating Group, 1-156, 2014.
1119 Schindler, D. W.: Evolution of phosphorus limitation in lakes, Science, 196, 260–262, 1977.
1120 Schitüter, L., Riemann, B., and Søndergaard, M.: Nutrient limitation in relation to phytoplankton
1121 carotenoid/chlorophyll a ratios in freshwater mesocosms, J. Plankton Res., 19, 891-906, 1997.
1122 Smayda, T. J.: Harmful algal blooms: their ecophysiology and general relevance to phytoplankton blooms in the sea,
1123 Limnol. Oceanogr., 42, 1137–1153, 1997.
1124 Steichen, J. L., Denby, A., Windham, R., Brinkmeyer, R., and Quigg, A.: A tale of two ports: Dinoflagellate and
1125 diatom communities found in the high ship traffic region of Galveston Bay, Texas (USA), J. Coastal Res., 31(2),
1126 407-416, 2015.
1127 Steichen, J. L., Windham, R., Hala, D., Kaiser, K., Labonte, J. M., Petersen, L. H., Bacosa, H., Bretherton, L.,
1128 Kamalanathan, M., Setta, S., and Quigg, A.: Rapid physicochemical and biological assessment of Galveston Bay in
1129 the wake of Hurricane Harvey, abstract#AI44D-3023, in: Ocean Sciences Meeting 2018, American Geophysical
1130 Union, Portland, Oregon, USA, February, 2018.
1131 Stramski, D., Reynolds, R. A., Kaczmarek, S., Uitz, J., and Zheng, G.: Correction of pathlength amplification in the
1132 filter-pad technique for measurements of particulate absorption coefficient in the visible spectral region, Appl.
1133 Optics, 54, 6763-6782, 2015.
1134 Suggett, D. J., Warner, M. E., Smith, D. J., Davey, P., Hennige, S., and Baker, N. R.: Photosynthesis and production
1135 of hydrogen peroxide by Symbiodinium (pyrrhophyta) phylotypes with different thermal tolerances 1, J. Phycol, 44,
1136 948-956, 2008.
1137 Suggett, D. J., Moore, C. M., Hickman, A. E., and Geider, R. J.: Interpretation of fast repetition rate (FRR)
1138 fluorescence: signatures of phytoplankton community structure versus physiological state, Mar. Ecol. Progr. Ser.,
1139 376, 1-19, 2009.
1140 Sun, D., Huan, Y., Qiu, Z., Hu, C., Wang, S., and He, Y.: Remote-sensing estimation of phytoplankton size classes
1141 from GOCI satellite measurements in Bohai Sea and Yellow Sea, J. Geophys. Res. Oceans, 122, 8309-8325, 2017.
1142 Thrane, J.-E., Kyle, M., Striebel, M., Haande, S., Grung, M., Rohrlack, T., and Andersen, T.: Spectrophotometric
1143 analysis of pigments: a critical assessment of a high-throughput method for analysis of algal pigment mixtures by
1144 spectral deconvolution, PloS one, 10, e0137645, 2015.
1145 Wang, G., Lee, Z., Mishra, D. R., and Ma, R.: Retrieving absorption coefficients of multiple phytoplankton
1146 pigments from hyperspectral remote sensing reflectance measured over cyanobacteria bloom waters, Limnol.
1147 Oceanogr., Meth., 14, 432-447, 2016.
1148 Wright, S. W., and Jeffrey, S. W.: Pigment markers for phytoplankton production, in: Marine organic matter:
1149 biomarkers, isotopes and DNA, The Handbook of Environmental Chemistry, edited by Volkman, J. K., Springer,
1150 Berlin, Heidelberg, Germany, 71-104, 2006.